A macro model for shallow foundations on granular soils describing non-linear foundation behavior

J. Tistel, G. Grimstad and G. R. Eiksund
Norwegian University of Science and Technology (NTNU), Trondheim, Norway

ABSTRACT: This paper describes a macro model for a shallow foundation. The macro model represents the non-linear soil structure interaction (SSI) exemplified by a suspension bridge anchor-block. The model can be adjusted and used for other structures. The formulation uses an elasto-plastic framework to calculate the foundation response. A yield surface in the $V - M$ - H (Vertical, Moment and Horizontal loading) load-space defines the yield and failure envelopes. A non-associated potential surface and a simple bi-linear hardening law describe the magnitude as well as the direction of the plastic displacements. Calibration of model parameters are performed through 2D and 3D finite element calculations. The model is suited for integration in a program for structural design. Compared to a full finite element model, the macro model simplifies the soil structure interaction analyses significantly. The yield and potential surfaces include the option to modify the shape in the $H - V$ plane versus the $M - V$ plane. Allowing for this flexibility in the formulation improves modelling of foundation uplift behavior. The paper demonstrates calibration of macro model parameters through a calculation example. Validation of the model by prototype testing in a sand bin is also performed and presented.

1 Introduction

1.1 *Bearing capacity and macro modeling*

Bearing capacity problems are one of the central topics within geotechnical engineering. The classical bearing capacity formulation presented by Terzaghi [1], further developed by e.g. Brinch-Hansen [2], Meyerhof [3] and others is commonly used for design purposes. Predictions using such methods depends nevertheless on a number of empirical factors. The response to a change in the load state may not be easily foreseen using the classical bearing capacity theories. These theories neither accommodate non-linearity as they are considered limit state methods Gottardi and Butterfield [4].

Several researchers have investigated models describing the foundation yield surface in a *V-M-H* (Vertical – Moment – Horizontal) space. The constitutive behavior of foundations subjected to loads or displacements is typically established based on a combination of theoretical/physical description and an experimental program. The observed response is used to describe a representative yield surface(s), potential surface(s) and hardening rule(s). Establishing the foundation yield/failure surface in the *V-M-H* space may accommodate a more efficient design process simplifying the interaction between geotechnical and structural design activities. Further, the macro model may replace the soil elements in an already comprehensive integrated Finite-Element Analysis (FEA) describing complex interactions between the various degrees of freedom. The relatively simple calculation routine (macro model) implemented in the structural program may thus save time and cost within a design process. This will nevertheless require a well-calibrated model.

This study presents first a literature review within the field of macro modeling; a proposed macro element for shallow foundations is thereafter described, followed by a description of the model parameters calibration process. The paper finally presents the validation of the model behavior. The use of the model is exemplified by an academic example investigating the response of a suspension bridge anchor block foundation subjected to load combinations in the *V-M-H* space. The macro model results are compared with Finite Element (FE) analyses results. The paper also presents experimental work performed to validate the model to a prototype foundation on dense to medium dense sand in a 4 m × 4 m × 3 m ($L \times B \times D$) sand-bin. Assumptions and uncertainties associated with the model are discussed.

This study makes use of yield formulations and ideas published by Martin [5], Houlsby and Cassidy [6], Cremer, et al. [7] and others. The model presented herein has non-associated flow. The yield and potential surfaces include the option to modify the shape in the $H - V$ load-plane separately from the $M - V$ load-plane. A flow rule and a hardening law describe the size and direction of the plastic displacements. Elastic model parameters are determined from three-dimensional (3D) FE analyses, whereas yield surface parameters, potential surface parameters and hardening parameters are determined from two-dimensional (2D) FE analyses. The model captures the whole range of $0 < V < V_{max}$, whereas the example focuses on a case where $V = V_{max}/30$.

1.2 *The ferry free E39 coastal route project*

The Norwegian Public Roads Administration (NPRA) is planning to upgrade the E39 coastal route in Norway, a distance of about 1100 km. Fixed links at seven fjord crossings along this route will replace ferry connections. The fjords widths ranges up to 5 km and the depths ranges up to 1300 m Dunham [8]. Large bridge structures will be required to cross the fjords. Construction of bridge structures at large water depths is found achievable by use of deepwater-offshore technology developed through decades of experience from the oil and gas industry. Several conceptual studies are executed for the different strait crossings:

- Large-span suspension bridges (main-span more than 3 km).
- End-anchored or side-anchored floating bridges of lengths more than 5000 m (Figure 1-1 and Figure 1-2).
- Multi-span suspension bridges on floating towers anchored by use of TLP (Tension-leg Platform) anchoring system at large depths (Figure 1-3).
- Submerged Floating Tube Bridge (SFTB), concrete tunnel floating some 20 m below the water surface. These are either anchored to seabed or connected to floating pontoons.

Figure 1-1. Side-anchored floating bridge (illustration quoted with permission from NPRA).

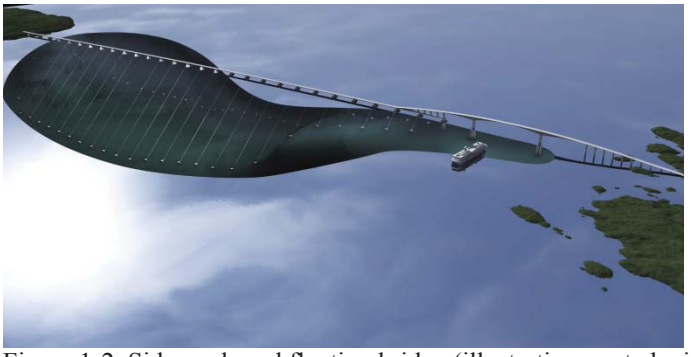

Figure 1-2. Side-anchored floating bridge (illustration quoted with permission from NPRA).

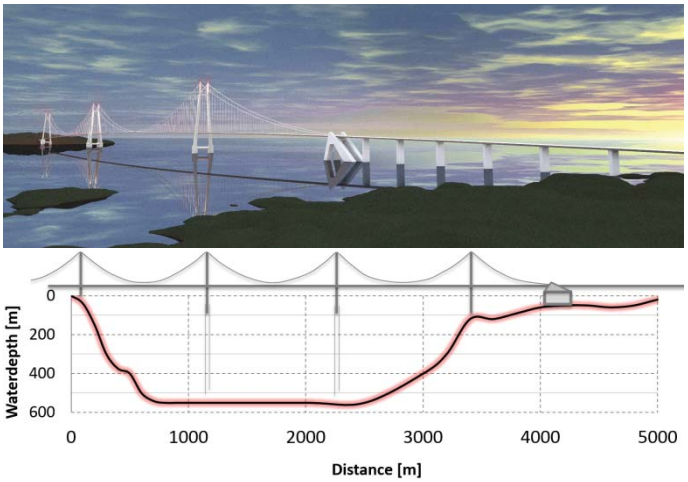

Figure 1-3. Multi-span suspension bridge with floating towers crossing Bjørnafjorden (illustration quoted with permission from NPRA).

Combinations of the different concepts may also be considered depending on the boundaries defined by the site, such as fjord width, depth and environmental conditions.

The geotechnical challenges concerns the foundations and anchoring of the different bridge alternatives. These may in many cases experience large permanent tension loads combined with cyclic load amplitudes. Several foundation and anchoring concepts may be viable for such structures: Gravity Based Structures (GBS), suction piles, combinations of gravity and suction piles (e.g. TLP anchors, Støve [9], Andersen [10]), fluke anchors, piles, rock anchors and more.

The new state route 520 floating bridge crossing Lake Washington (Seattle) is more than 2 km long. Bored piles, fluke anchors and gravity structures are used to anchor the mooring lines along the bridge axis, Howard, et al. [11]. On the other hand, end-anchored floating bridges do not utilize anchors along the bridge axis. These bridges are designed with an arch shape, transferring the loads to the bridge abutments either as compression or tension loads. Solland, et al. [12] and Meaas, et al. [13] describe the design of the Salhus bridge and the Bergsøysund bridge. These bridges are 1250 m and 900 m long respectively, and spans across water depths of up to 500 m. The abutments transfer the forces to the ground (rock) by a combination of gravity and permanent rock anchors.

A combination of a suspension bridge and a fixed bridge is one of the concepts under evaluation for one of the crossings along the E39 route (e.g.Figure 1-3). The suspension bridge can be constructed by several main spans across the deep part of the fjord (4 km length), whereas a fixed bridge constitutes the remaining distance to the shoreline (≈1 km).

1.3 *Anchor block for suspension bridge main cables*

Design of the offshore structures for anchoring the main cables of the suspension bridge is challenging. The cable pull may be in the range of 1 GN for the largest bridges, in comparison it is 1.2 GN for the Akashi Kaikyo bridge, Yasuda, et al. [14]. For the current study, the main-cable anchor might be located offshore at water depths between 30–70 m.

A comparable design is previously erected by the completion of the Storebælt east bridge in 1997. The anchor structure for the main cables were constructed in dry docks, and towed to site followed by installation. The structures were ballasted with iron ore, olivine and sand to achieve the necessary on-bottom weight (1.9 GN) Hededal and Sørensen [15]. This method of construction sequences are similar to the methodology used for offshore GBS structures installed in the north Sea. The Storebælt cable anchors are installed at approximately 12 m water-depths on gravel pads above clay till.

This paper is an extended and improved version of the conference paper Tistel and Grimstad [16]. The model presented within this paper suggests a calculation methodology to ease and improve the design process for surface foundation structures on granular materials. The model suitability is exemplified with a calculation example concerning a main cable anchor block foundation on dense sand. The model might be even more useful for higher mobilized foundations experiencing a larger degree of non-linearity, e.g. extreme loads on gravity anchors for a variety of floating structures; floating bridges, ocean fish farms, vessels and so on.

The model presented here represents a new application of the macro model concept which was pioneered within the offshore industry. The methodology has previously been developed and used for jack-up spudcan foundations (e.g. Houlsby and Cassidy [6], Bienen and Cassidy [17]), pipelines (e.g. Tian and Cassidy [18]), SEPLA anchors (e.g. Cassidy [19]) and more.

2 Literature review

Bearing capacity is one of the central topics within geotechnical engineering. The well known bearing capacity formulation put forward by Terzaghi [1] and presented in Eq. (1) may provide satisfactory predictions of the bearing capacity for shallow foundations.

$$q = \frac{Q}{BL} = c \cdot N_c + \gamma \cdot D \cdot N_q + \gamma \cdot B \cdot N_\gamma \cdot \frac{1}{2} \tag{1}$$

Where B = width of foundation, L = length of foundation, D = depth of foundation, c = cohesion of soil, γ = effective unit weight of soil, N_c, N_q, N_γ are bearing capacity factors which depend mainly on the friction angle in the soil. Several commonly used bearing capacity formulations are based on the formulation proposed by Terzaghi, examples of these being suggested by Brinch-Hansen [2], Meyerhof [3] and others. The methodology described by Brinch-Hansen [2] is a commonly used methodology within offshore foundation design. Predictions using such methods depend nevertheless on a number of empirical factors. The interface between foundation design and structural design may require significant attention as the results from such methods may not be easily foreseen. Several iterations between the design disciplines may also be necessary, as the bearing capacity calculation needs to be updated based on changes in loads, load inclination and so on.

This section describes a literature review on the topic of macro models describing the behavior of foundations resting on soil. The review covers the following central topics; interaction diagrams, failure surfaces, swipe tests and plasticity based models. A significant amount of high quality work is performed within this field, and extractions of this work are presented here.

2.1 *Interaction diagrams*

The need for appurtenant adjustment-factors concerning load eccentricity, load inclination, foundation geometry, etc. led to the interest in interaction diagrams for foundations under planar loading Gottardi and

Butterfield [4]. According to Cassidy, et al. [20] this way of interpreting soil structure interaction was first suggested by Roscoe & Schofield (1957) and further developed by Butterfield (1980, 1981). Vertical load eccentricity and inclined loads are reduced to three load components acting at the center of the foundation underside illustrated in Figure 2-1 together with corresponding displacements.

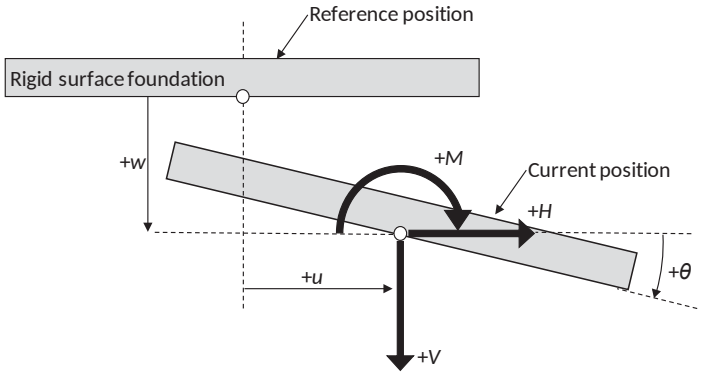

Figure 2-1. Loads and corresponding displacement components in a plane strain condition. Directions according to Butterfield, et al. [21].

It may be convenient to make the forces non-dimensional. The forces are thus normalized by the bearing capacity for pure vertical load, V_{max}, and the moment is also divided by the width of the foundation for this purpose. The force and displacement vector **S** and **v** are thus expressed by Eq. (2) corresponding to the standardization suggested by Butterfield, et al. [21].

$$\mathbf{S} = \begin{bmatrix} V/V_{max} \\ M/(B \cdot V_{max}) \\ H/V_{max} \end{bmatrix} = \begin{bmatrix} v \\ m \\ h \end{bmatrix}, \quad \mathbf{v} = \begin{bmatrix} w \\ B\theta \\ u \end{bmatrix} \tag{2}$$

Interaction diagrams define a region inside which all allowable load combinations must lie. Several experimental studies are executed to define such yield envelopes; these are performed for foundations on both sand and clay. Experimental tests on a 100 mm by 500 mm prototype foundation on dense sand (relative density D_r = 85 %) in laboratory environment are performed by Gottardi and Butterfield [4]. Results from laboratory tests are used to define interaction diagrams in loading component planes within the *V - M/B – H* space. They applied a parabolic shape of failure envelopes expressed by Eq. (3) and Eq. (4).

$$\frac{H}{V_{max}} = 0.48 \frac{V}{V_{max}} \left[1 - \frac{V}{V_{max}} \right]^{\beta} \tag{3}$$

$$\frac{M}{B \cdot V_{max}} = 0.36 \frac{V}{V_{max}} \left[1 - \frac{V}{V_{max}} \right]^{\beta} \tag{4}$$

Where *V – M/B* and *H* represents vertical load, moment load (normalized by foundation width) and horizontal loading, V_{max} is the foundation maximum bearing capacity under pure vertical load, and β = 1. The tests confirmed maximum horizontal and moment capacity found in previous studies, H/V_{max} = 0.12 and $M/(B*V_{max})$ = 0.09. Interaction curves generated by Eq. (3) and Eq. (4) are plotted and presented in Figure 2-2.

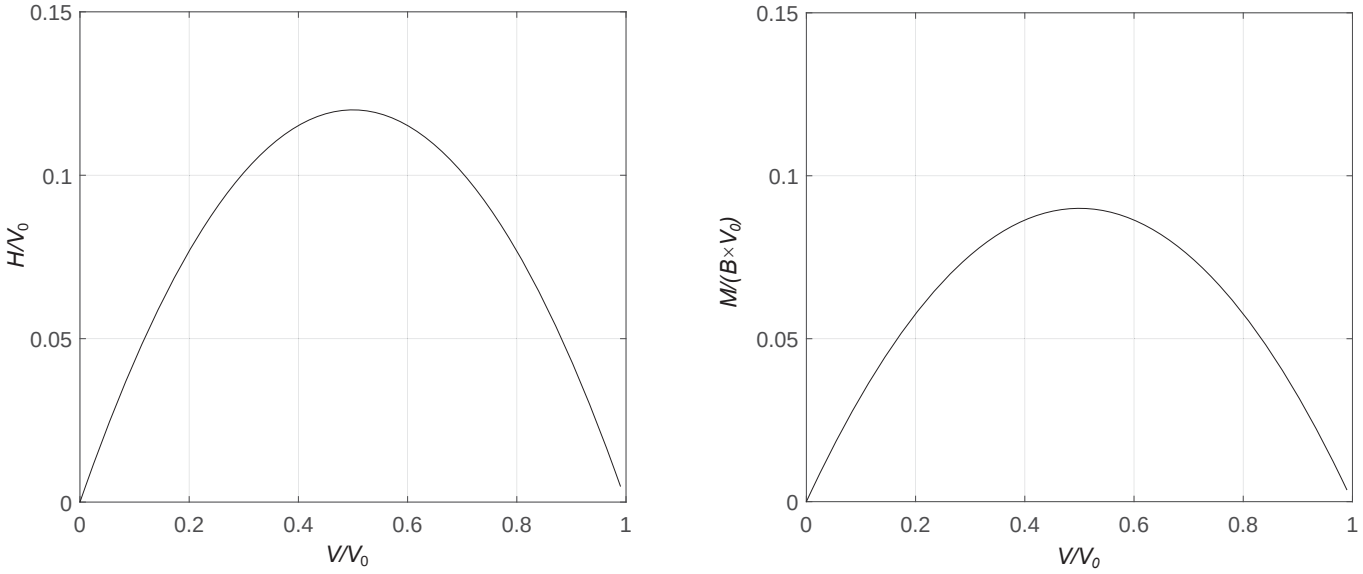

Figure 2-2. Interaction diagrams in *H-V* and (*M/B*) – *V* plane.

Interaction diagrams based on laboratory tests and published data were earlier presented by Georgakis and Butterfield [22], they concluded the same numbers for maximum H/V_{max} and $M/(B*V_{max})$, being 0.12 and 0.09 respectively. Experimental testing and belonging interaction diagrams found from literature shows that the maximum values of H/V_{max} and M/BV_{max} occurred at $V = V/V_{max} = 0.5$, as shown in Figure 2-2. Gottardi and Butterfield [4] also observed an increase in horizontal capacity if a negative moment was applied as opposed to applying a positive moment (when *H* in Figure 2-1 is positive). This is the basis for the eccentricity in the *H – M/B* plane discussed later (eccentricity factor *a*). The eccentricity in the *M/B – H* plane is not recognized in commonly used formulations e.g. Brinch-Hansen [2]. Other publications exploring the shape of interaction curves (or yield surface) are Gottardi, et al. [23], Nova and Montrasio [24], Byrne and Houlsby [25], Byrne and Houlsby [26], Martin [5], Martin and Houlsby [27], Cassidy, et al. [28], Cheng and Cassidy [29] and others.

2.2 *Three dimensional failure surface*

According to Houlsby [30], Butterfield and Ticof [31] were the first to present a three dimensional yield surface for combinations of vertical, moment and horizontal loads. Three dimensional failure surfaces are developed through interaction diagrams based on the intrinsic foundation behavior. Butterfield and Gottardi [32] presented a three dimensional failure envelope for shallow footings on sand. The shape of the normalized failure envelopes led to the derivation of Eq. (5), which is a combination of Eq. (3) and Eq. (4) but now also including the afore mentioned eccentricity within the *H – M/B* plane.

$$\left(\frac{H}{t_h}\right)^2+\left(\frac{M}{Bt_m}\right)^2-\frac{2aMH}{Bt_ht_m}=\left[\frac{V}{V_{max}}\left(V_{max}-V\right)\right]^2 \tag{5}$$

Where t_h and t_m control the initial slope of the yield surface in the *H - V* and *M/B - V* plane respectively, and also the maximum value of *H* and *M*. *a* is an eccentricity factor, correcting the yield surface in the *H – M/B* plane.

Martin [5] suggested a modified form of the yield surface. Previous equations by Nova and Montrasio [24] (Eq. (4) and Eq. (5)) are limited in that of the rounding off effect to occur at $V/V_0 = 1$, β must be less than unity. This in turn means that the location of the peak horizontal (or moment) load can only be shifted from $V/V_0 = 0.5$ towards $V/V_0 = 1$. Observations from laboratory tests on spudcan foundations in clay implied that the peak values of both H/V_0 and $M/(BV_0)$ occur when $V/V_0 < 0.5$. Martin [5] therefore introduced a second variable exponent, β_2, and included the parameter μ in the expression for a representative yield surface quoted in Eq. (6).

$$f=\left(\frac{H}{h_0\cdot V_0}\right)^2+\left(\frac{M/B}{m_0\cdot V_0}\right)^2-\frac{2\cdot a\cdot H\cdot M/B}{h_0\cdot m_0\cdot V_0^2}-\mu\cdot\left(\frac{V}{V_0}\right)^{2\beta_1}\cdot\left(1-\frac{V}{V_0}\right)^{2\beta_2}=0 \tag{6}$$

Where h_0 and m_0 represent H_{max}/V_0 and $(M_{max}/(B*V_0)$ respectively, a is the eccentricity parameter in the $H - M/B$ plane, β_1 and β_2 are shape parameters. Since each change in β_1 and β_2 affects the magnitude as well as the location of the peak, the parameter μ is adjusted to preserve the desired peak horizontal load:

$$\mu = \left[\frac{(\beta_1 + \beta_2)^{(\beta_1+\beta_2)}}{\beta_1^{\beta_1} \cdot \beta_2^{\beta_2}} \right]^2 \tag{7}$$

The effect of β_1 and β_2 is illustrated in Figure 2-3, showing the yield surface within the $H - V$ plane. The dotted line represents the yield surface applying $\beta_1 = \beta_2 = 0.99$, the continuous line represents the yield surface applying $\beta_1 = 0.7$ and $\beta_2 = 0.99$.

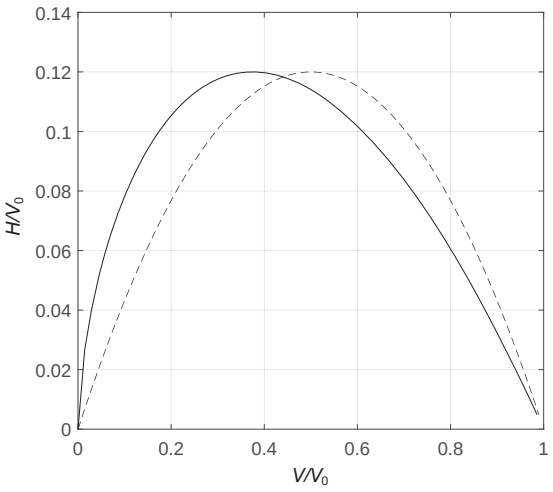

Figure 2-3. Yield surface in $V - H$ plane illustrating the effect of β_1 and β_2.

A complete yield surface in $V - M/B - H$ space described by Eq. (6) is presented in Figure 2-4. The surface within the figure applies $\beta_1 = \beta_2 = 0.99$, $a = -0.2$, $h_0 = 0.12$ and $m_0 = 0.09$. The effect of the mentioned eccentricity factor a is seen in Figure 2-5.

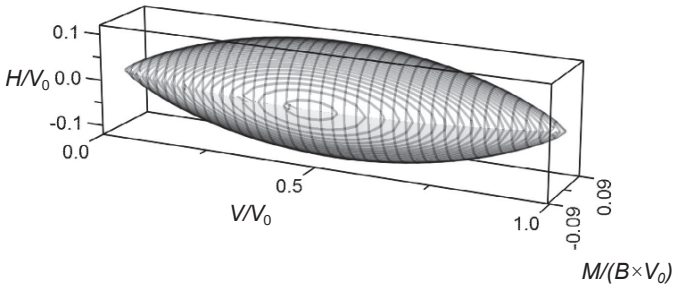

Figure 2-4. Yield surface based on formulation suggested by Martin [5].

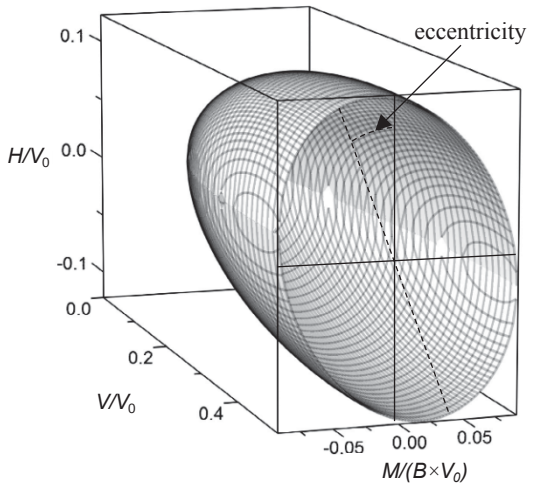

Figure 2-5. Cross section at $V = V_{max}/2$, illustrating eccentricity in the $H - M/B$ plane.

If it is found most appropriate to use different variable exponents (β-values) in the $V{-}H$ plane and $V{-}M/B$ plane, the formulation published by Cremer, et al. [7] can be used. Their study presents a macro model capable of integrating the effects of soil yielding, but also of the foundation uplift (separation between soil and foundation) at the foundation interface. This is further discussed in the section concerning plasticity based models.

2.3 *Swipe tests*

According to Houlsby and Cassidy [6] and others, swipe tests can be performed to determine the yield surface for an embedment in the V - M/B - H space. In a swipe test, the footing is load-controlled in the vertical direction until it reaches a prescribed load. Rotation or horizontal displacement is then applied while the vertical displacement is fixed. The trace of the forces corresponds to a track along the yield surface.

A detailed assessment of the swipe test methodology to define a set of yield loci defining the yield surface is presented by Gottardi, et al. [33]. Both laboratory tests and numerical simulations are discussed within the paper. Sources of errors such as deformations in the test rig and elastic deformations during swipe tests might affect the observed behavior in a laboratory test. Elastic deformations may occur because V is decreasing. $dw = 0$ is a boundary condition during the test, $dw = dw^e + dw^p$ and hence $dw^e \neq 0$ implies that $dw^p \neq 0$. For such a condition, the yield loci will expand. A similar expansion may occur due to elastic deformation of the loading frame. The trace of the forces will reflect this expansion and the initial V_0 may not be representative. Gottardi, et al. [33] conclude that errors may be corrected if the vertical elastic displacements are known and if they are small. If the hardening parameter depends also on $d\theta^p$ and du^p in addition to w^p, the concept of $w^p = 0$ swipe testing is no longer valid. However, according to literature laboratory testing reveals a limited V_0 dependency of $d\theta^p$ and du^p. Numerical analyses may be used to perform swipe tests. Sources of errors encountered in a laboratory test will diminish in a numerical model e.g. rig stiffness and problems of soil replication.

Figure 2-6 illustrates two load paths in swipe tests: The foundation is loaded to a vertical load V_0, whereafter the foundation is fixed in vertical translation and rotation or horizontal translation. Thereafter either a horizontal displacement or rotation is imposed on the foundation. The resulting forces constitute traces in the $V - M/B - H$ space and define the yield surface.

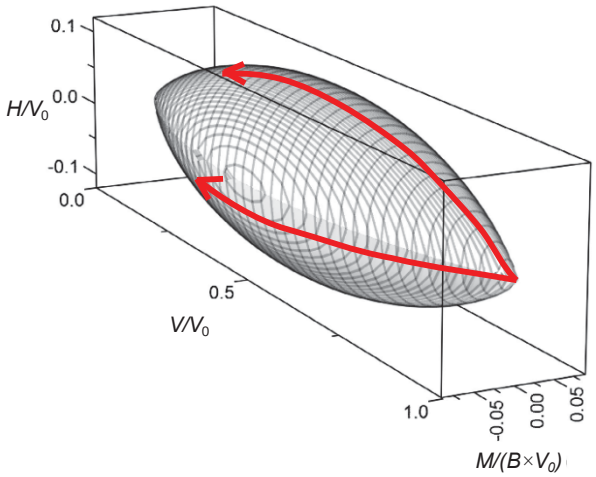

Figure 2-6. Illustration of load paths in a swipe test

2.4 *Plasticity based models (macro models)*

Plasticity-based analyses may be constructed in terms of the force resultants acting on the footings and the corresponding footing displacements Gottardi, et al. [23]. Classical plasticity theory is used to model a non-linear response to loads acting on a foundation. Key assumptions needed in order to establish a non-linear model could be as follows:

- A principle for adding elastic and plastic contributions:
  Total displacement (**U**) = elastic displacement + plastic displacement => d**U** = d**U**^{e} + d**U**^{p}
- A relationship that governs the elastic contribution: d**U**^{e} = $\boldsymbol{D}^{-1}$·d**F**, where $\boldsymbol{D}$ = elastic stiffness matrix, d**F** is the load increment

Ingredients necessary to control the plastic contribution are:

- A yield criterion
- A flow rule
- A hardening rule
- Potential surface if non-associated model

2.4.1 *Elastic region*

A yield surface describes a region in which a load state can exist in the *V- M/B – H* space. Changes in the load state occurring within this region is considered to be elastic. The relationship between load application and elastic displacement can be expressed in the form of a matrix equation presented in Eq. (8) Ngo-Tran [34], Houlsby [30].

$$\begin{pmatrix} V/GD^2 \\ M/GD^3 \\ H/GD^2 \end{pmatrix} = \begin{bmatrix} k_1 & 0 & 0 \\ 0 & k_2 & k_4 \\ 0 & k_4 & k_3 \end{bmatrix} \begin{pmatrix} w/D \\ \theta \\ u/D \end{pmatrix} \tag{8}$$

Where G is the shear modulus in the soil, D is the diameter of a circular foundation and $k_{1\text{-}4}$ are dimensionless stiffness parameters. The diagonal terms represent stiffness in vertical and horizontal translation as well as rotation.

The k_4 parameter represents the coupling between rotation and horizontal translation. The assessment of the k_4 parameter varies; Cremer, et al. [7] do not include the cross coupling stiffness parameter in their study of a shallow foundation. They argue that the exclusion of the cross coupling can be done for surface foundations since the values of the cross coupling stiffness parameters are low. The contribution to the foundation response will therefore be marginal. Houlsby [30] argues that the k_4 significance needs to be properly assessed. The importance of the k_4 term will depend on the structure geometry and the selection of load reference point. Semi-empirical solutions or FE may be used to determine the dimensionless stiffness parameters.

The cross coupling stiffness for structures subjected to dynamic loads is treated by several researchers, a few of these studies are referred to here. The literature review reveals that coupling is generally agreed to be insignificant for a surface foundation on a homogeneous half-space, whereas coupling exists for embedded foundations and foundations on layered soil. Veletsos and Wei [35] present numerical data for the steady-state response of a rigid circular footing supported at the surface of an elastic half-space. The footing is excited by a harmonically varying horizontal force and a harmonically varying overturning moment. The response quantities

evaluated include the displacements of the disk in the directions of the exciting forces, the rotation due to the horizontal force, and the distributions of the contact stresses beneath the disk. A simplified solution where the off-diagonal terms of the flexibility matrix are assumed to be zero is also evaluated. The resulting stiffness coefficients in horizontal translation and rotation are thereafter compared to an exact solution whereafter it is concluded that the difference between the simplified and exact solution is found to be negligible for practical purposes. The coupling between horizontal translation and rotation is thus found to be insignificant.

The study presented by Bu and Lin [36] considers the coupled horizontal-rocking response of embedded square foundations. The study reveals an increasing coupling stiffness with increasing embedment ratio, E/B, where E = embedment depth and $2B$ = width of the square foundation. The cross coupling term is low for frequency factors close to zero compared to horizontal and rocking stiffness.

Research on dynamic soil-structure interaction for offshore wind turbine foundations are presented by Liingaard, et al. [37] and Andersen and Clausen [38]. Liingaard, et al. [37] evaluate the dynamic soil–structure interaction of suction caissons for offshore wind turbines. The investigations include evaluation of the vertical and coupled sliding–rocking vibrations, influence of the foundation geometry and examination on the properties of the surrounding soil. The authors conclude that the two coupling terms between sliding and rocking are equal, i.e. $K_{HM}^{0} = K_{MH}^{0}$ (static stiffness coefficients), within the accuracy of the analysis. The authors conclude further that the effects of increasing the skirt length enlarge with depth with respect to the rocking impedance and the sliding-rocking coupling components.

Andersen and Clausen [38] investigated the particular problem of a rigid foundation on a layered subsoil. Based on the Green's function for a stratified half-space, the impedance of a surface footing with arbitrary shape is computed. The authors demonstrate that soil layering has to be taken into consideration when dynamic response of a structure is to be determined. They also conclude that the fatigue lifespan of a wind turbine structure installed on a layered soil profile may be incorrectly predicted if the layered soil profile is modeled by a simple ground model based on a homogeneous half-space.

2.4.2 *Plastic behavior*

When the load state touches and expands the yield surface, plastic displacements occur. The hardening law is used to define this plastic response. The flow rule defines the direction or ratio of the flow (plastic deformation), and is defined by the following expression:

$$\left[dw^{p}, du^{p}, B \cdot d\theta^{p}\right] = d\lambda \cdot \left[\frac{\partial Q}{\partial V}, \frac{\partial Q}{\partial H}, B \cdot \frac{\partial Q}{\partial M}\right] \tag{9}$$

Where: dw^{p}, du^{p}, $B \cdot d\theta^{p}$ are plastic deformations, $d\lambda$ is the plastic multiplier which defines the magnitude of the plastic displacement increment and Q is the plastic potential function (potential surface). If the model is associated the potential surface and the yield surface is the same surface. If the model is non-associated, there is a separate potential surface, Q. The plastic incremental displacement vector is directed along the normal to the potential surface (illustrated in Figure 2-7). This surface must therefore be adjusted to match the observed behavior from either large scale tests, laboratory testing, or FE analyses.

If the model is associated, a simple approach may be to apply a simple correction factor on the derivatives to match the observed plastic displacements, and thereby use the yield surface equation as the plastic potential. The publications by Martin [5] and Cassidy, et al. [20] concludes that, for their study (spudcan foundations for jack-up structures), an associated flow rule is adequate for flow in the *H-M/B* plane. However, they corrected the plastic displacement in the vertical direction by using a factor to adjust the size of the vertical displacements. Experimental results and fit of plastic potentials for shallow foundations in sand are further presented in publications by Cassidy, et al. [39], Cassidy [40], Cheng and Cassidy [29].

Figure 2-7 presents a yield and potential surface in the *H-V* plane. The direction of the plastic flow in horizontal and vertical direction is given by dQ/dH and dQ/dV respectively.

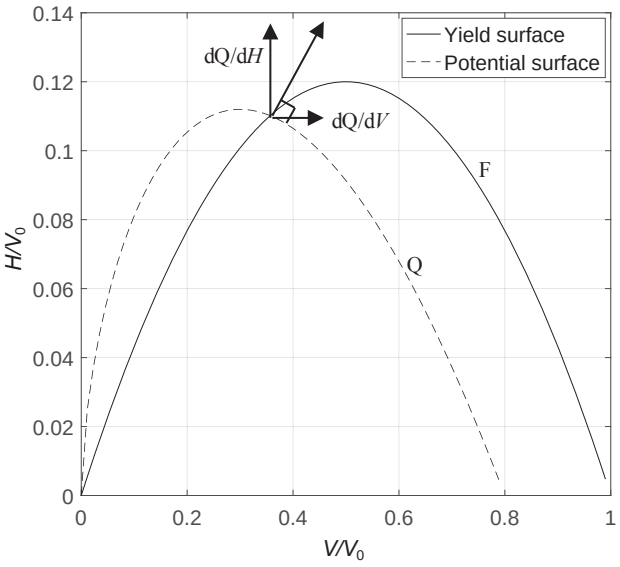

Figure 2-7. Example of yield surface (F) and potential surface (Q) in the $H - V$ plane.

Cremer, et al. [7] modelled the mechanism of yielding and uplift through a global separated but coupled plasticity-uplift model. Theoretically, the structure should move downwards (positive w increments) as long as the effective width ranges between: $B/2 < B_{\text{effective}} < B$. However, when the effective width is lower than $B/2$, the vertical displacement shall be directed upwards (negative w increments).

The hardening provides the resistance against plastic deformation and the hardening law relates the development of plastic strains to an expansion, a translation or some other movement of the yield surface. The hardening law determines the size of the plastic strain increment. The plastic deformations U_p increase with the load state or mobilization. The vertical plastic displacement w^p is commonly used as the one and only direction controlling the hardening for spudcan considerations Cassidy, et al. [20]. Depending on the problem, the plastic displacements in rotation and translation (radial hardening) may also affect the hardening of the yield surface. The topic of radial hardening is also discussed by Cassidy, et al. [28]. The yield surface may increase with increasing mobilization, accompanied by plastic deformations until, depending on the soil conditions, the maximum bearing capacity is reached.

3 Macro model calibration and implementation

This section describes the framework for a macro model prepared for a shallow foundation on sand. The model applies the theories presented in section 2 and demonstrates the model by an analytical calculation example. The example considers static loading on a suspension bridge anchor block foundation. The macro model is calibrated against FE results, whereafter the model precision is demonstrated by comparing to FE results for other load combinations. The model is calibrated to the foundation size and soil conditions used in the example case.

The aim of this paper is to present the macro model, to show the calibration towards either FE or laboratory results, and to assess the precision of the model. The calibration is performed by use of 3D FE for interpretation of elastic parameters, while a 2D FE code is applied for interpretation of yield surface, potential surface and hardening parameters.

3.1 *Calculation case*

This section describes the structural geometry, weights and soil conditions for the calculation example used to demonstrate the macro model. The anchor block foundation geometry will in general depend on the local site conditions; water depths, soil/rock properties, environmental loads, bridge geometry/span width, structural weight, traffic loads etc. In addition, construction issues, esthetical impact, marine operations, will also affect the design in terms of materials, geometry and weight.

The following parameters apply for the calculation example:

- Main cable-pull 500 MN
- Anchor block foundation dimensions: Rectangular, $B \times L$ = 100 m × 50 m
- Self-weight = 2 GN
- Water depth at the anchor block location: 40 m
- Height from the cable fixation to the underside of the foundation base: 60 m and 106 m (two load cases)
- Main cable inclination angle with horizontal plane: α = 10° - 15°
- Ground conditions: 50 m dense sand over bedrock. 32° friction angle in the sand, and elastic shear modulus, G = 80 MPa

The static cable-pull component is the dominating load component acting on the anchor block. Dynamic loads are significantly lower and therefore not included within this example. Vortex loads and buffeting loads on the bridge system in addition to wave loads acting on the anchor block surface are assumed to cause cable forces an order of magnitude lower than the static cable-pull. The calculation of the foundation response is therefore considered as a static system within this example. Figure 3-1 shows the outline of the anchor block.

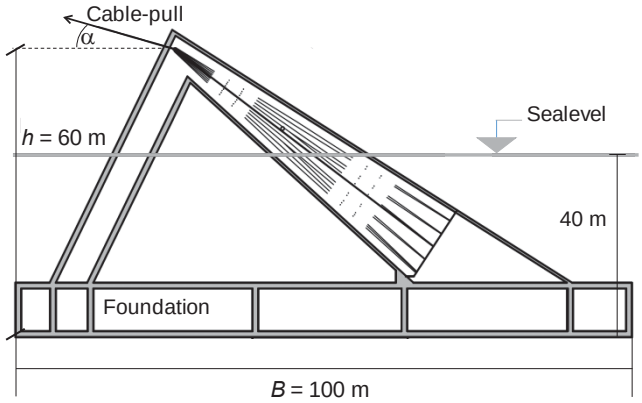

Figure 3-1.Anchor block. (not in scale).

3.2 *FE analyses*

The FE code Plaxis (www.plaxis.nl) is used to calibrate the model. Both 3D and 2D analyses are used:

- 3D linear elastic analyses are used to determine the dimensionless stiffness parameters k_1, k_2, k_3 and k_4 presented in Eq. (8)
- 2D analyses are used to determine the yield surface, potential surface and hardening parameters.

If the foundation in question is a strip foundation, the maximum bearing capacity, V_{max}, may be calculated by 2D analyses. If the foundation is a 3D problem (i.e. Length × width does not categorize as a strip foundation) V_{max} can be calculated either by use of classic theory e.g. Mayerhof Brinch-Hansen [2] or by use of 3D FE.

The complete calibration could be performed in 3D, the combined analysis method is however computationally faster. A 3D failure analysis would also require significant amount of elements in order not to have significant overshoot. The 2D analysis is regarded to provide reasonable results to be used for determination of the shape of the yield and potential surfaces.

3.2.1 *Linear elastic analysis – 3D FE*

The 3D model utilizes 10-noded linear elastic elements. The dimensionless stiffness factors in vertical translation, rotation and horizontal translation are derived by use of this model. The coupling between rotation and horizontal translation, k_4, is also evaluated. Constant stiffness with depth is implemented in the model. The material parameters used in the model are presented in Table 1. The soil layer thickness is 50 m above bedrock. The model is presented in Figure 3-2. The foundation plate is made infinitely stiff representing a rigid foundation, this is a simplification which is considered to be satisfactory for the purpose of this paper which is to demonstrate the macro model.

Table 1. Linear elastic parameters in 3D FE analysis.

Parameter	Value	Unit	Description
$\gamma_{saturated}$	20	[kN/m^3]	Saturated unit weight
E	216	[MN/m^2]	Young's modulus
ν	0.35	[-]	Poisson's ratio
G	80	[MN/m^2]	Shear modulus
E_{oed}	347	[MN/m^2]	Constrained Young's modulus

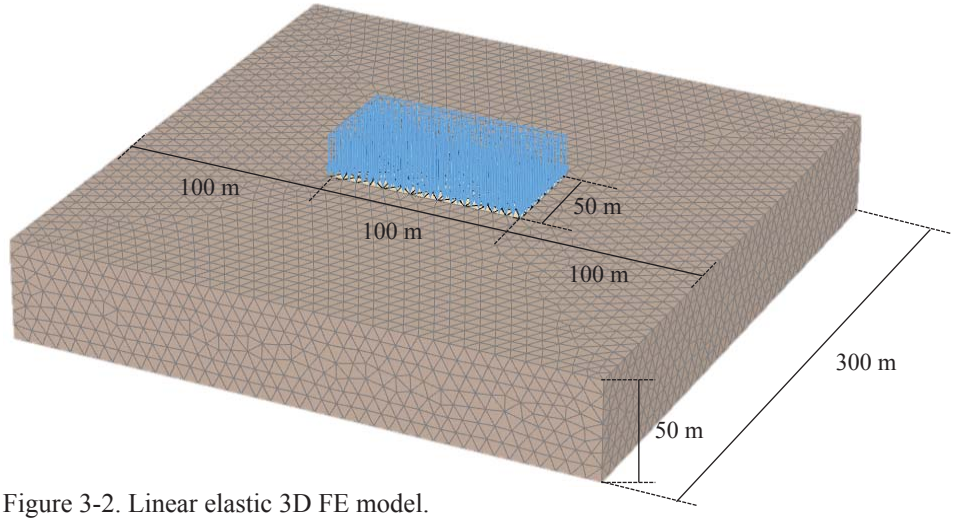

Figure 3-2. Linear elastic 3D FE model.

3.2.2 *2D FE analyses*

The calibration of the yield surface, potential surface and hardening parameters are performed based on a plane strain 2D FE analysis. 15 noded elements are used and a linear elastic – perfect plastic Mohr Coulomb (MC) soil model is used. While a hardening soil (HS) model (Schanz and Vermeer [41]) in many cases represents the sand behavior more precisely, the MC model is found satisfactory to illustrate the calibration and precision of the macro model. The material parameters are presented in Table 2, and the model geometry is shown in Figure 3-3. It should be noted that the applied dilation angle ψ is somewhat low, and a higher value is recommended. Typical values of ψ is in the range of φ – 30 degrees.

Table 2. Mohr Coulomb soil material parameters used in 2D FE analyses.

Parameter	Value	Unit	Description
$\gamma_{saturated}$	20	[kN/m^3]	Saturated unit weight
E	216	[MN/m^2]	Young's modulus
ν	0.35	[-]	Poisson's ratio
G	80	[MN/m^2]	Shear modulus
E_{oed}	347	[MN/m^2]	Constrained Young's modulus
c'_{ref}	5	[kN/m^2]	Cohesion
φ'	32	[degrees]	Internal friction angle
ψ	0	[degrees]	Dilatancy angle

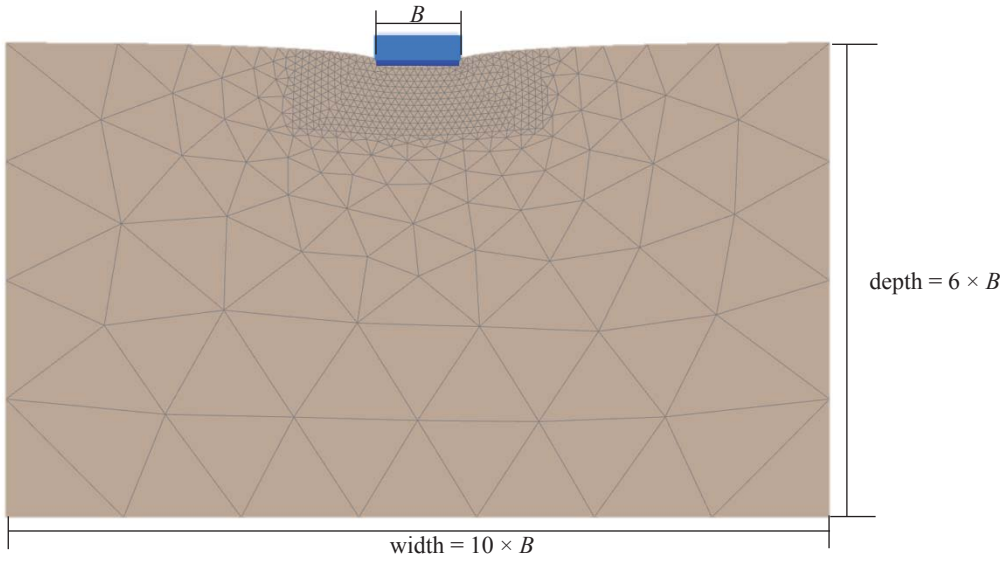

Figure 3-3. 2D FE model.

The foundation is modelled with an infinitely stiff plate, representing a rigid foundation. Vertical load is applied by evenly distributed forces, while moments are imposed on the structure by a pair of vertical forces in opposite direction at each side of the foundation and thereby acting around the foundation center. Horizontal forces are applied at the center of the foundation at mudline level.

3.3 *Macro model*

This section describes the macro model framework and the calibration of the model parameters. The anchor block example is used as a practical case to illustrate the calibration process and the model precision. A stepwise description of the model is provided in terms of: yield surface, elastic behavior and plasticity.

The designation of forces and displacements and directions of these are made according to the standardization suggested by Butterfield, et al. [21] (presented in Figure 2-1). The forces are applied at the center of the base of the foundation, and the behavior (kinematic displacements) of the soil-structure interaction system are also extracted from the center of the foundation. The forces are denoted as, V, M/B and H, and displacements as w (vertical), $B \cdot \theta$ (differential displacement between foundation edges due to rotation) and u (horizontal). The forces are normalized by the maximum bearing capacity under pure vertical load, V_{max}. The load vector (**S**) and displacement vector (**v**) defined by Eq. (2) are thus adopted for this study.

3.3.1 *Yield surface*

The yield surface defines a region within only elastic displacements will occur. The yield surface may expand with an increasing load state. Any expansion of the yield surface leads to a plastic displacement. The yield surface may increase until the ultimate state is reached, describing the ultimate failure surface. The macro model applies a combination of the yield surface used by Martin [5], expressed by Eq. (6), and the yield surface used by Cremer, et al. [7]. The yield surface applied within this study is described by Eq. (10) – Eq. (16).

$$F = H_F^2 + M_F^2 - N_F^2 - V_F^2 = 0 \tag{10}$$

Where:

$$H_F^2 = \left(\frac{H}{h_0 \cdot V_0}\right)^2 \cdot \left(\frac{\mu_m}{\mu_h}\right)^2 \cdot \left(\frac{V}{V_0}\right)^{2(\beta_{1m}-\beta_{1h})} \cdot \left(1-\frac{V}{V_0}\right)^{2(\beta_{2m}-\beta_{2h})} \tag{11}$$

$$M_F^2 = \left(\frac{M/B}{m_0 \cdot V_0}\right)^2 \tag{12}$$

$$N_F^2 = \frac{2 \cdot a \cdot H \cdot M / B}{h_0 \cdot m_0 \cdot V_0^2} \cdot \frac{\mu_m}{\mu_h} \cdot \left(\frac{V}{V_0} \right)^{(\beta_{1m} - \beta_{1h})} \cdot \left(1 - \frac{V}{V_0} \right)^{(\beta_{2m} - \beta_{2h})} \tag{13}$$

$$V_F^2 = \mu_m^2 \cdot \left(\frac{V}{V_0} \right)^{2\beta_{1m}} \cdot \left(1 - \frac{V}{V_0} \right)^{2\beta_2 m} \tag{14}$$

$$V_0 = \kappa \cdot V_{\max} \tag{15}$$

κ is a state parameter defining the degree of mobilization, finally μ_h and μ_m are defined by:

$$\mu_h = \frac{\left(\beta_{1h} + \beta_{2h}\right)^{(\beta_{1h} + \beta_{2h})}}{\beta_{1h}^{\beta_{1h}} \cdot \beta_{2h}^{\beta_{2h}}}, \qquad \mu_m = \frac{\left(\beta_{1m} + \beta_{2m}\right)^{(\beta_{1m} + \beta_{2m})}}{\beta_{1m}^{\beta_{1m}} \cdot \beta_{2m}^{\beta_{2m}}} \tag{16}$$

Where h_0 and m_0 represents H_{max}/V_{max} and $(M_{max}/B)/V_{max}$ respectively, a is the eccentricity parameter in the $H - M/B$ plane, β_1 and β_2 are shape parameters. V_{max} is defined by 2D FE analysis, h_0, m_0, β_1 and β_2 are interpreted from swipe tests.

Swipe tests are performed in a 2D FE code applying the anchor block foundation geometry as illustrated in Figure 3-3. The swipe tests are performed with one degree of freedom, i.e. only rotation or only translation, while fixation is applied in the other two directions. The test results reveal that horizontal forces are generated when rotation is imposed on the structure, whereas no moments occur at imposed translation. Figure 3-4 presents the swipe tests in the V - M/B - H space. The calibrated yield curves (surface) generated by the macro model is plotted together with the test results.

Figure 3-5 shows the complete yield surface in the $V - M/B - H$ load-space defined by the calibrated parameters. The resulting yield surface parameters appears as follows; $h_0 = 0.12$, $m_0 = 0.09$, $\beta_{1h} = 0.88$, $\beta_{2h} = 0.85$, $\beta_{1m} = 0.91$ and $\beta_{2m} = 0.95$. $V_{max} = 70$ GN.

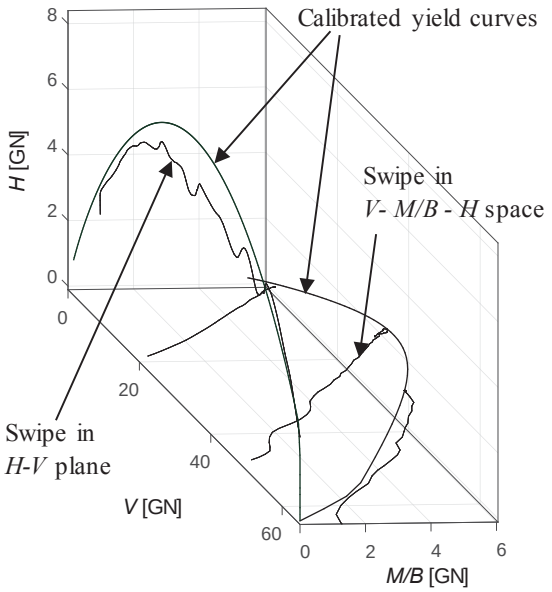

Figure 3-4. Swipe tests in $H - V$ plane and in $V - M/B - H$ space.

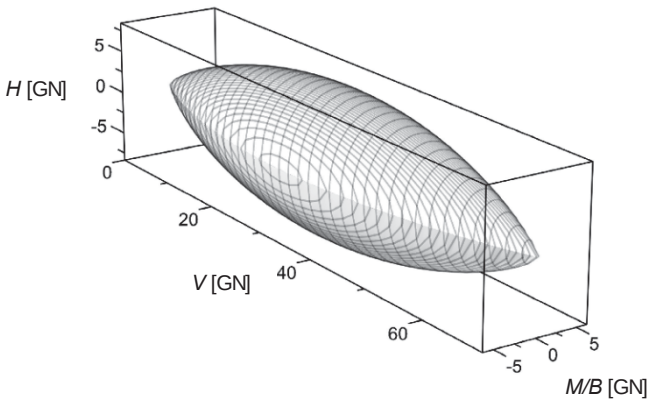

Figure 3-5. 3D representation of the calibrated yield surface used in the macro model.

The eccentricity factor, a, is investigated by analyzing load cases with different $H/(M/B)$ ratios. According to literature, there shall be an eccentricity factor of approximately a = -0.2. The problem defined by the suspension bridge anchor block foundation represents however a case where the load components H and M/B are deemed to follow a load path within the positive H and M/B sector. It is therefore emphasized to find a best fit within this sector. The best fit to the FE results for V/V_{max} = 1/35, matching the results within the positive H and M/B sector is achieved with a = 0, the yield surface is presented in Figure 3-6 a). If it is expected that the foundation will experience negative moments, one should consider to apply an eccentricity factor, a, in the order of -0.15 to -0.2. The yield surface generated by applying an eccentricity factor a = -0.15 is presented in Figure 3-6 b).

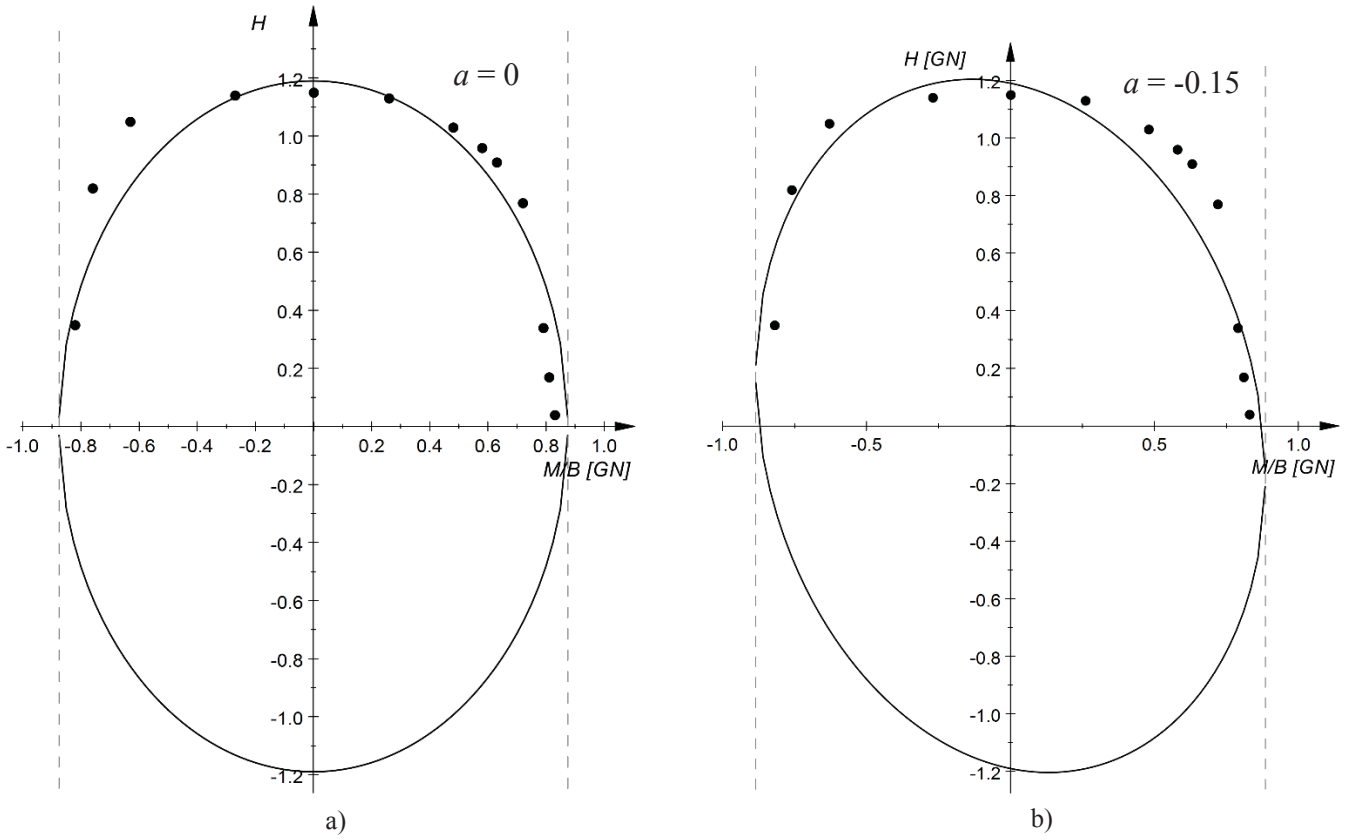

Figure 3-6. Yield surface at V = 2 GN. Yield surface with eccentricity factor: a) a = 0, b) a = -0.15.

The script uses an implicit iteration as the model evaluates the flow rule after application of the displacement or load step. Every single iteration step starts by a trial step. The yield surface equation defines also a surface outside the range $0 < V < V_0$. Therefore, a "cap" surface, that ensures that the loading state stays within the defined range of V, is introduced. The cap is defined by the ellipsoidal surface, G, defined by Eq. (17). The cap (ellipsoid) limits the value of V to be within the requirement $0 < V < V_0$ both on the minimum boundary and at the maximum boundary. In fact, the ellipsoid ensures that all load steps are within the surface described by the surface G (Figure 3-7). If the load state is outside the cap, $G_{trial} > 0$ (see Figure 3-7), the

loads (*V,M/B, H*) or displacements (*w, Bθ, u*) are reduced by a secant iteration methodology as described by Eq. (18) by use of the β factor defined in Eq. (19), this iterative procedure is continued until G ≈ 0.

$$G = H^2 + \left[\frac{M}{B}\cdot\frac{h_0}{m_0}\right]^2 - \frac{\mu^2\cdot V\cdot\left(V_0 - V\right)}{V_0^2} \tag{17}$$

$$\left(V, \frac{M}{B}, H\right) = \left(V_0, \frac{M_0}{B}, H_0\right) + \beta\cdot\left[\left(V_1, \frac{M_1}{B}, H_1\right) - \left(V_0, \frac{M_0}{B}, H_0\right)\right] \tag{18}$$

$$\beta = \beta_1 - \frac{-G_0}{\left(G_1 - G_0\right)}\cdot\left(\beta_1 - \beta_0\right) \tag{19}$$

Where:

- μ is a factor defining the height and width of G
- G_0 is the solution of Eq. (17) for the loading combination of the former step.
- G_1 is the solution of Eq. (17) for the current loading combination.

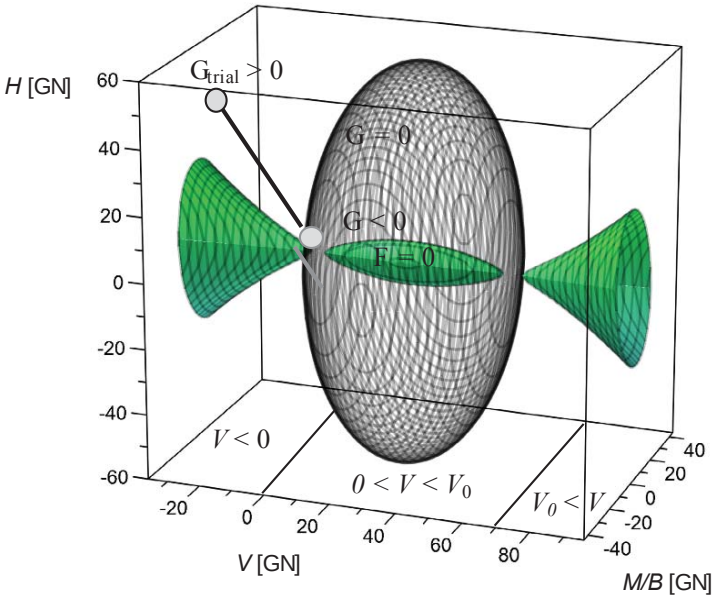

Figure 3-7. Yield surface F plotted together with "cap" function G for $0 < V < 60$ GN, $V_0 = V_{max}$ and $\mu = 2$ for illustration purposes.

3.3.2 *Elastic Behavior*

The soil response within the yield surface is elastic, and defined by the shear modulus, *G*, and dimensionless elastic stiffness factors. Cross coupling between the horizontal translation and rotational displacements is also represented by a factor (k_4) in the matrix.

The representation of the coupling between rotation and horizontal translation may be debated as discussed in section 2.4.1. Cremer, et al. [7] and Houlsby [30] recommends to do a proper assessment of the effect of the coupling. Analyses performed using the model presented in section 3.2.1 reveals the following: For an elastic half-space of infinite depth, there will be a cross coupling between rotational and translational elastic movement. However, when the depth from the foundation base to a significantly stiffer layer (bedrock) is limited, the cross coupling is found to be insignificant. This is verified through 3D FE analysis. The three degree of freedom elastic behavior is expressed by Eq. (20) which is essentially equal to Eq. (8), only replacing *D* (diameter) by *B* (foundation width), and evaluating load-displacement increments instead of the total load and displacement. The elastic increments calculated by Eq. (20) are further used when extracting the plastic deformations as expressed in Eq. (29) - (31).

$$\begin{pmatrix} dV \\ \dfrac{dM}{B} \\ dH \end{pmatrix} = GB \begin{bmatrix} k_1 & 0 & 0 \\ 0 & k_2 & k_4 \\ 0 & k_4 & k_3 \end{bmatrix} \begin{pmatrix} dw^{el} \\ Bd\theta^{el} \\ du^{el} \end{pmatrix} \tag{20}$$

Where G = the elastic shear modulus in the soil, k_1, k_2, k_3, k_4 are dimensionless stiffness factors, in vertical, rotation, horizontal, and coupling between rotation and translation. These factors are determined by interpretation of 3D FE calculation results. The results show that there is no coupling between horizontal and moment loading for this problem. The k_4 factor is therefore equal to zero for the case study. The resulting dimensionless parameters are; $k_1 = 5.62$, $k_2 = 0.61$, $k_3 = 2.51$, $k_4 = 0$.

If linear elastic 3D analyses are not performed, one may use analytical stiffness relations for a rectangular foundation defined by e.g. Pais and Kausel [42] presented in Eq. (21) to Eq. (23):

$$k_1 = \frac{Gb}{1-\nu}\left[3.1 \cdot \left(\frac{a}{b}\right)^{0.75} + 1.6\right] \cdot \frac{1}{G \cdot B} \tag{21}$$

$$k_2 = \frac{Gb^3}{1-\nu}\left[3.73 \cdot \left(\frac{a}{b}\right)^{2.4} + 0.27\right] \cdot \frac{1}{G \cdot B^3} \tag{22}$$

$$k_3 = \frac{Gb}{2-\nu}\left[6.8 \cdot \left(\frac{a}{b}\right)^{0.65} + 0.8 \cdot \left(\frac{a}{b}\right) + 1.6\right] \cdot \frac{1}{G \cdot B} \tag{23}$$

Where the rectangular foundation is described by the area $2a \times 2b$ and $b < a$, ν is the Poisson's ratio, G is the shear modulus in soil and the last part of the equations, i.e. $(1/(GB)$ and $1/(GB^3))$ is added to accommodate the dimensionless k factors presented in Eq. (20). Correction of the stiffness parameters is necessary due to the limited depth to bedrock. The correction is performed by use of Eq. (24) – Eq. (26), Gazetas [43]:

$$k_{1\,cor.} = \left[1 + 1.3 \cdot \frac{r_{0\,eq}}{d}\right] \tag{24}$$

$$k_{2\,cor.} = \left[1 + \frac{1}{6} \cdot \frac{r_{0\,eq}}{d}\right] \tag{25}$$

$$k_{3\,cor.} = \left[1 + \frac{1}{2} \cdot \frac{r_{0\,eq}}{d}\right] \cdot \tag{26}$$

where d is depth to bedrock below foundation base, the parameter $r_{0\,eq}$ represents an equivalent radius which is calculated by Eq. (27) for translation and by Eq. (28) for rotation, Gazetas [44], Wolf [45]. The bedrock is assumed infinitely stiff for this case.

$$r_{0\,eq} = \sqrt{\frac{A_0}{\pi}} \tag{27}$$

$$r_{0\,eq} = \sqrt[4]{\frac{4I_0}{\pi}} \tag{28}$$

Dimensionless elastic stiffness parameters are also calculated by the semi-empirical approximation presented by Gazetas [43] for: 1) rigid circular foundation (with equivalent radius) and 2) rectangular surface foundation. Both 1) and 2) are corrected by $k_{1\text{cor.}}$, $k_{2\text{cor.}}$ and $k_{3\text{cor.}}$ respectively (Eq. (24) – Eq. (26)). The formulas presented by Gazetas [43] are not quoted here but can be found in the reference.

Table 3 presents the calculation of dimensionless stiffness parameters based on the three methodologies previously described. The 3D FE result is also presented. Table 4 presents the ratio between the dimensionless stiffness parameters calculated by semi-empirical expressions and 3D FE analysis.

Table 3. Dimensionless stiffness parameters calculated by semi-empirical expressions and 3D FE analysis.

Stiffness parameter	Pais and Kausel [42 Wolf [45] rectangle [-]	Gazetas [43] circular disk [-]	Gazetas [43] rectangle [-]	3D FE [-]
k_1	5.34	5.00	5.16	5.62
k_2	0.56	0.53	0.52	0.61
k_3	2.94	2.71	2.87	2.51

Table 4.Ratio between stiffness parameters calculated by semi-empirical expressions and 3D FE analysis.

Stiffness parameter	Ratio: Pais and Kausel/3DFE [-]	Ratio: Gazetas-circular disk/3DFE [-]	Ratio: Gazetas-rectangle/3DFE [-]
k_1	0.95	0.89	0.92
k_2	0,92	0.86	0.85
k_3	1.17	1.08	1.14

One may note that the semi-empirical expressions over-predict the horizontal translation stiffness parameter k_3, whereas the vertical translation and rotation stiffness, k_1 and k_2, are under-predicted comparing to the 3D FE result. Further, the best match for k_1 and k_2 is achieved by the methodology presented by Pais and Kausel [42] (rectangular foundation), whereas best match for k_3 is achieved by the methodology presented by Gazetas [43] for a circular disk with equivalent radius calculated by Eq. (27) and Eq. (28).

In order to capture the 3D effect of the base plate load-displacement relationship, elastic deformations from 3D analyses are combined with the plastic deformations from 2D analyses. The 2D FE plastic displacements are separated from the total displacements by Eq. (29) to Eq. (31). These equations are used when producing the combined 3D and 2D FE response considered as the "true" response.

$$dw^p = dw - dw^{el} = dw - \frac{dV}{k_1 \cdot B \cdot G} \tag{29}$$

$$Bd\theta^p = Bd\theta - Bd\theta^{el} = Bd\theta - \frac{dM_2}{B^2 \cdot G \cdot k_2} \tag{30}$$

$$du^p = du - du_3^{el} = du - \frac{dH}{k_3 \cdot B \cdot G} \tag{31}$$

Where $k_4 = 0$ (the terms including k_4 are therefore excluded from the equations).

3.3.3 *Plasticity*

In this case study, the anchor block will be subjected to a large horizontal force and corresponding overturning moment. Uplift of the foundation center may occur for large moments, as discussed in Cremer, et al. [7]. Uplift of the center point is initiated when the effective width becomes lower than $B/2$. Whereas uplift was previously modelled as a global separated but coupled plasticity-uplift model, discussed in section 2.4.2, the uplift mechanism is now integrated in the model through calibrated potential surface parameters. The potential surface described by Eq. (32) includes the possibility to model the uplift of the foundation center. The equation is in its form identical to the equation for the yield surface. However, it uses different coefficients h_0, m_0 and a and a different factor β to match the plastic deformations;

$$\mathrm{Q} = \mathrm{H}_\mathrm{Q}^2 + \mathrm{M}_\mathrm{Q}^2 - \mathrm{N}_\mathrm{Q}^2 - \mathrm{V}_\mathrm{Q}^2 = 0 \tag{32}$$

Where:

$$\mathrm{H}_Q^2 = \left(\frac{H}{h_{0p} \cdot V_{0p}}\right)^2 \cdot \left(\frac{\mu_{mp}}{\mu_{hp}}\right)^2 \cdot \left(\frac{V}{V_{0p}}\right)^{2\left(\beta_{1mp} - \beta_{1hp}\right)} \cdot \left(1 - \frac{V}{V_{0p}}\right)^{2\left(\beta_{2mp} - \beta_{2hp}\right)} \tag{33}$$

$$M_Q^2 = \left(\frac{M/B}{m_{0p} \cdot V_{0p}} \right)^2 \tag{34}$$

$$N_Q^2 = \frac{2 \cdot a \cdot H \cdot M/B}{h_{0p} \cdot m_{0p} \cdot V_{0p}^2} \cdot \frac{\mu_{mp}}{\mu_{hp}} \cdot \left(\frac{V}{V_{0p}} \right)^{(\beta_{1mp} - \beta_{1hp})} \cdot \left(1 - \frac{V}{V_{0p}} \right)^{(\beta_{2mp} - \beta_{2hp})} \tag{35}$$

$$V_Q^2 = \mu_{mp}^2 \cdot \left(\frac{V}{V_{0p}} \right)^{2\beta_{1mp}} \cdot \left(1 - \frac{V}{V_{0p}} \right)^{2\beta_{2mp}} \tag{36}$$

The parameter V_{0p} is solved for the current state from requiring Q = 0. μ_{hp} and μ_{mp} are defined by similar expressions as in Eq. (16). Figure 3-8 presents the potential surface. Where the inclination parameters of the surface, and thereby the peak location can be chosen independently in the *H-V* plane and the *M/B-V* plane, as for the yield surface.

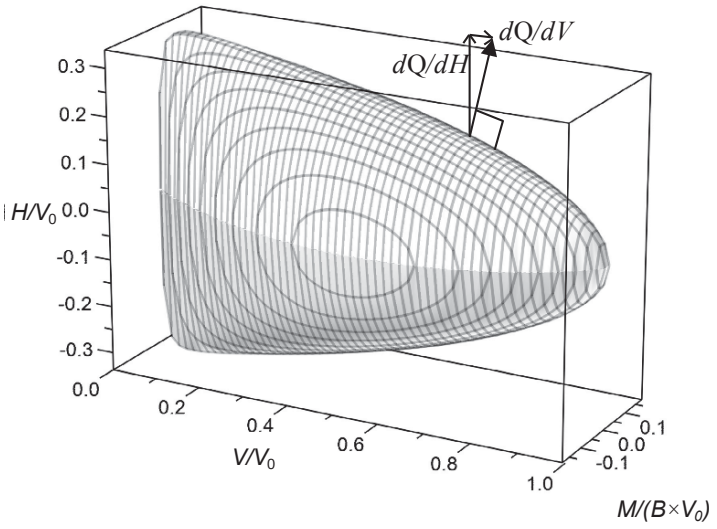

Figure 3-8. Potential surface.

The direction of the vertical displacement is dependent on the size of the moment loading. When the effective width is lower than *B*/2, the vertical displacement shall be directed upwards (negative *w* increments). The effective width equals *B*/2 when *M*/*B* equals:

$$\frac{B_{effective}}{B} = 1 - 2 \cdot e \cdot \frac{1}{B} \Rightarrow 0.5 = 1 - 2 \cdot \frac{M/B}{V} \Rightarrow M/B = V \cdot 0.25 \tag{37}$$

The *w*-direction shall be directed downwards when $M/B \leq 0.25V$ accordingly.

The shift in *w*-direction is modelled by the combination of potential surface parameters providing the correct direction of plastic flow (h_{0p}, m_{0p}, a_p, β_{1hp}, β_{1mp}, β_{2hp} and β_{2mp}). β_{1mp} *and* β_{2mp} control the direction of *w* at low *H/(M/B)* ratios. These two parameters should therefore be paid attention to accommodate uplift behavior. The direction of plastic displacement in *w* direction for large *H/(M/B)* ratios should be positive (with reference to Figure 2-1). The shape of the yield surface should therefore slope downwards towards V_0 in the whole range of $0 < V < V_0$ in the $H - V$ plane. This explains also why an associated model could not be applied for this problem. The conflicting shape requirements in the $H - V$ and $M/B - V$ plane shows the necessity of splitting β_1 *and* β_2 into β_{1hp}, β_{1mp}, β_{2hp} and β_{2mp}.

The parameters are calibrated to fit the direction of the plastic flow defined by FE analyses, five load cases with a broad spectra of *H/(M/B)* load paths are used in the calibration. The *H/(M/B)* ratios used in the calibration

of the potential surface are; *H/(M/B)* = 0.43, 1.07, 1.43, 1.65 and 2.15. Calibration of parameters may be performed by sum of least squares fitting algorithms, or by manual fitting.

Figure 3-9 illustrates the shift in the direction of vertical plastic displacements at different constant *H/(M/B)* load paths. The figure shows that the shift in vertical direction appears for $M/B \approx 0.25V - 0.3V$. This is in agreement with Eq. (37), showing that uplift starts at $M/B \approx 0.25V$. This behavior is modelled by the potential surface and all included in one formulation.

Figure 3-10 presents overturning moment versus rotation ($B\theta$). The calibrated model fits reasonably well with the FE model, especially within the most probable *H/(M/B)* ratios for the anchor block case which is in the range of $1 < H/(M/B) < 2$. The model over-estimates the moment capacity slightly for low *H/(M/B)* ratios. This deviation is however explained by the yield surface, which exceeds the FE result for low *H/(M/B)* ratios (Figure 4-3).

Figure 3-11 shows horizontal force with horizontal displacement. The calibrated model shows a good match with FE calculation results. Finally, the calibrated potential surface parameters are presented in Table 5.

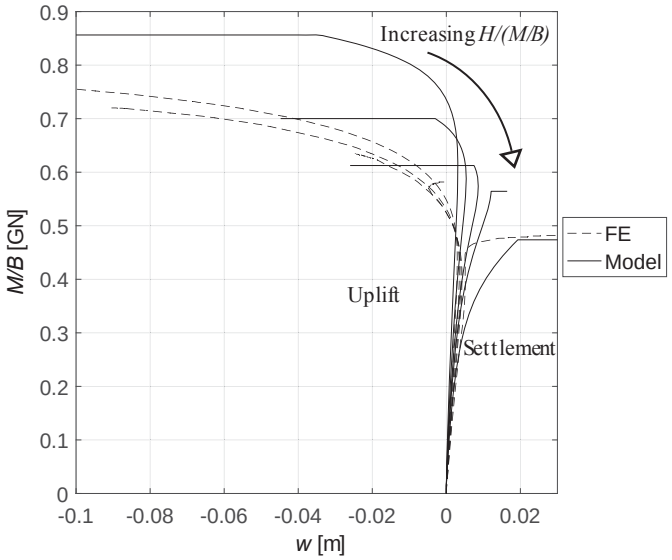

Figure 3-9. Overturning moment *M/B* [GN] versus vertical deformation *w* [m].

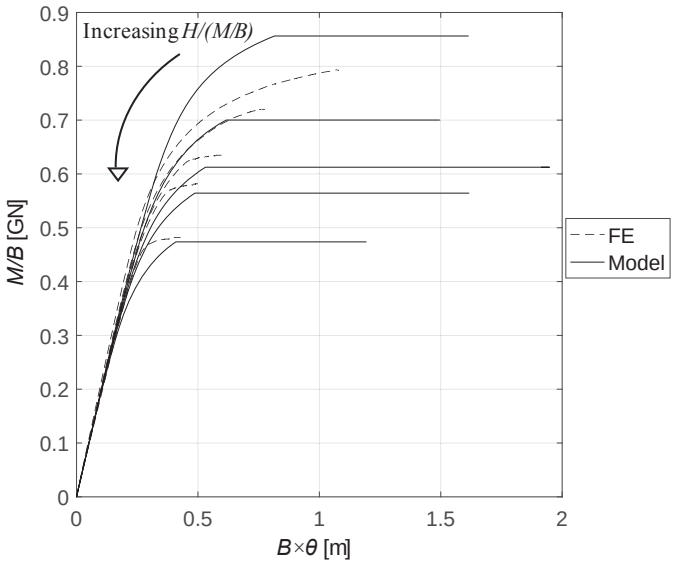

Figure 3-10. Overturning moment *M/B* [GN] versus foundation rotation $B\theta$ [m].

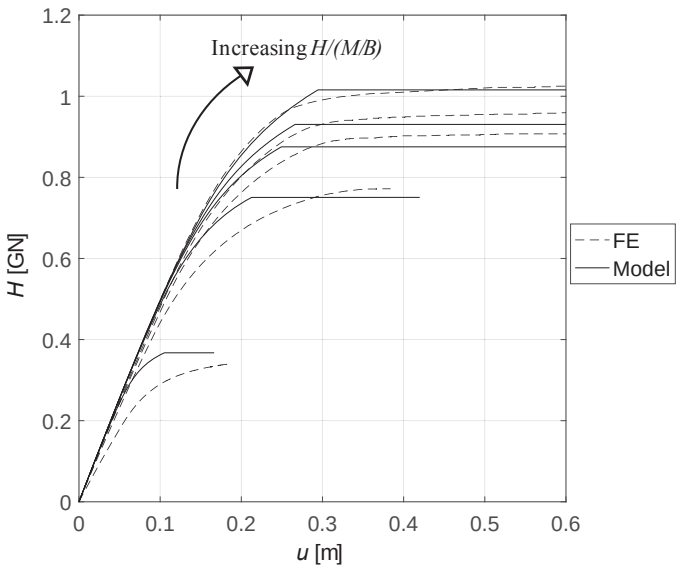

Figure 3-11. Horizontal force H [GN] versus horizontal displacement u [m].

The hardening law is defined by curve-fitting to FE calculation results. In order to match a broad range of load combinations within the *H/(M/B)* plane, two load cases are investigated when developing the hardening law. One case where *H/(M/B)* = 2.15, and one case where *H/(M/B)* = 1.07. The plastic displacement increments from the FE analysis are plotted against the degree of mobilization κ. The hardening curve shows a somewhat bi-linear trend in a plot of κ versus U_p for *H/(M/B)* = 1.07, and therefore a bi-linear hardening curve is chosen to describe the development of plastic displacement with increasing mobilization, expressed in Eq. (38).

$$\kappa(U_p) = \kappa_0 + a_h \cdot \frac{U_p}{B} \tag{38}$$

Where:

- $\kappa(U_p)$ is the mobilization (state parameter) at the current load condition
- κ_0 is the initial value of the state parameter, the mobilization when plastic strains are initiated.
- a_h is a curve fitting parameter
- U_p is the combined plastic displacement and is expressed in Eq. (39)

The combined plastic displacement increment, dU_p, is calculated by use of the following equation:

$$dU_p = C_1 \cdot du^p + C_2 \cdot \left(B \cdot d\theta\right)^p + dw^p \tag{39}$$

C_1 and C_2 weights the importance of plastic increments in rotation and horizontal translation. The concept of using C_1 and C_2 is inspired by Byrne and Houlsby [25].

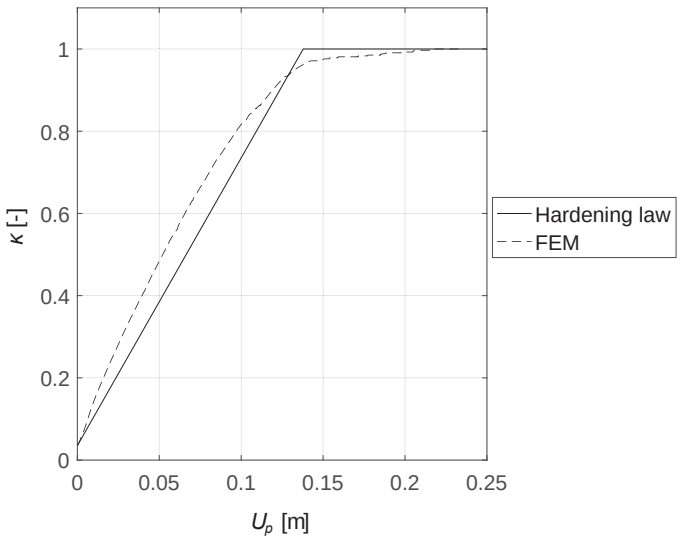

Figure 3-12. Hardening law versus 2D FEA result, *H/(M/B)* = 1.07.

The hardening parameters κ_0, a_h, C_1 and C_2 are optimized to fit the FE calculation result. The hardening curve is plotted in Figure 3-12. The choice of C_1 and C_2 determines which range of *H/(M/B)* one would prefer to fit. The characteristic of the κ versus U_p curve is more non-linear for a load case where H is more dominating. A hyperbolic function can be used if it is deemed necessary.

Table 5. Calibrated macro model parameters.

Yield surface		Potential surface		Elastic stiffness		Hardening	
h_0	0.12	h_{0p}	0.35	G	0.08 GPa	κ_0	0.035
m_0	0.09	m_{0p}	0.14	k_1	5.62	a_h	700
a	0.0	a_p	0	k_2	0.61	C_1	0.5
β_{1h}	0.88	β_{1hp}	0.01	k_3	2.51	C_2	0.4
β_{2h}	0.85	β_{2hp}	0.5	k_4	0		
β_{1m}	0.91	β_{1mp}	0.67				
β_{2m}	0.95	β_{2mp}	0.8				
V_{max}	70 GN						

4 Model parameters and validation

4.1 *Model Validation – Practical example*

The model is calibrated for a variety of *H/(M/B)* load paths, this is shown in Figure 3-9 to Figure 3-11. A practical calculation example is performed using an offshore anchor block as a case study. Dimensions, weights loads and soil conditions are outlined in section 3.1. The macro model parameters outlined in Table 5 is applied in the calculation. The load cases are presented in Table 6 and represent three different load paths in the $V - M/B - H$ space. Figure 4-1 shows the calculation result compared with the FE analysis result. The maximum capacities compare well, the degree of plasticity shows a reasonable fit. The model also shows a correct uplift response (case 3 shows negative w direction). It must be noted that the vertical displacements are rather small, and any deviation from the FE-curve presented in Figure 4-1 might appear severe while it may be considered minor compared to the foundation size.

The calculation is run to failure, and the numerical results are presented in Table 6. Where ΔV is the applied vertical force. V in Figure 4-1 includes foundation weight.

Table 6. Calculation cases. α is the main cable inclination, h is the vertical distance between main cable fixation and foundation.

	Case 1	Case 2	Case 3
α [°]	10	15	15
H/(M/B)	1.95	2.15	1.07
h [m]	60	60	106.6
Results:	Case 1	Case 2	Case 3
ΔV	-0.16	-.24	-0.19
H [GN]	0.92	0.91	0.69
M/B [GN]	0.47	0.42	0.64

If the main cable load is 500 MN, assuming 10 degrees cable angle with horizontal (Case 1), the deformations will be as follows: w = -0.8 mm (uplift), $B \cdot \theta$ = 60 mm, u = 29 mm.

The ability to model foundation uplift (with reference to the foundation center), is demonstrated by a simple calculation of the same foundation, applying a pure overturning moment. Failure (tilting) occurs accordingly when $M/B = 0.5 \cdot V = 1.0$ GN (for infinite bearing capacity). The moment (*M/B*) is limited by the bearing capacity. The macro model calculation approaches an asymptotic value of approximately *M/B* = 0.9 GN. Figure 4-2 presents the result using the same parameters as before.

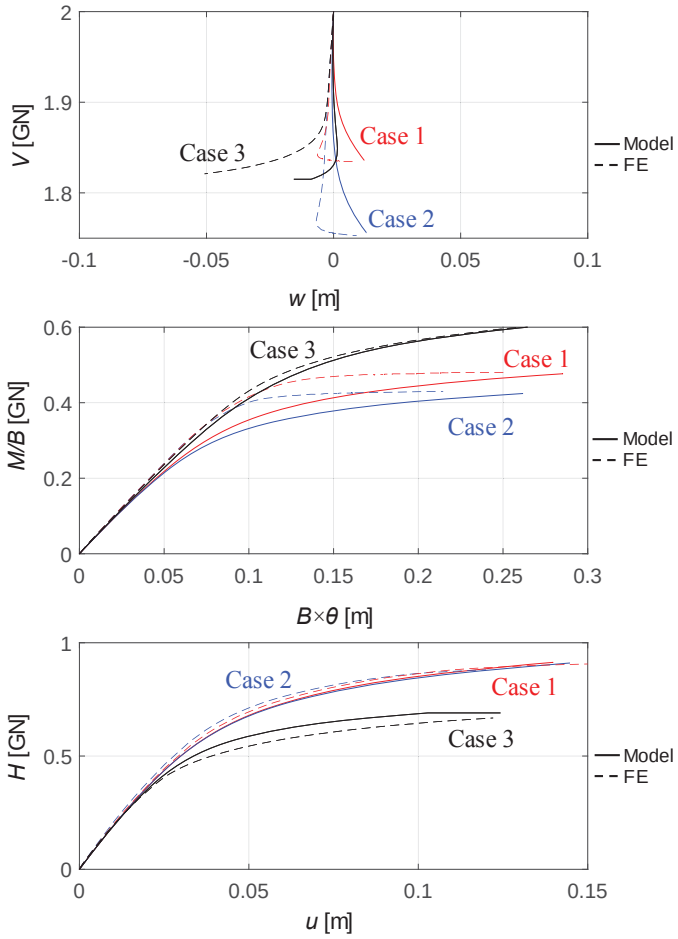

Figure 4-1. Comparison between FE analysis (dashed lines) and model results (continuous lines) for case 1, 2 and 3.

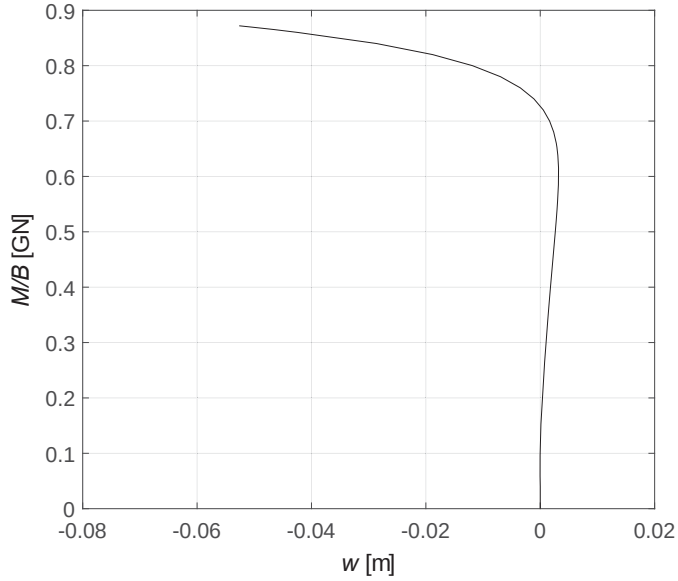

Figure 4-2. Foundation uplift validation.

4.2 *Model sensitivity, assumptions and limitations*

The yield surface is defined by the swipe tests in *V-H* and *V-M/B* plane, while the potential surface parameters are defined by the flow directions found from the FE result. This section discuss sensitivities in parameters related to: Elastic domain, yield surface and plasticity.

4.2.1 *Elastic domain*

The elastic parameters depends on the foundation aspect ratio (L × B) and the soil stiffness. The dimensionless stiffness parameters k_1, k_2, k_3, k_4 and G must therefore be updated with other foundation aspect ratios or varying soil conditions e.g. soil layering and anisotropic stiffness. The parameters may either be found by use of FE analysis, or analytical expressions e.g. Eq. (21) to (23).

4.2.2 *Yield surface*

The yield surface is defined by calibration to either laboratory tests or FE analyses as presented in the preceding sections. The surface is generic, meaning that the same surface parameters govern the whole range of foundation weight (W) within $0 < W < V_{max}$. It also means that the same surface parameters may be used for different foundation sizes, as long as V_{max} is adjusted to the foundation size. Gottardi, et al. [33] refers to several tests performed for various aspect ratios and soil conditions revealing constant h_0 and m_0 (= H_{max}/V_{max} and $M_{max}/(BV_{max})$) = 0.123 and 0.09 respectively. This also means that V_{max} is the only parameter governing yield and potential surface which needs to be changed with varying soil parameters or soil layering for isotropic strength conditions. The yield surface parameters dependency on anisotropic soil strength are not evaluated within this study, this should be addressed if anisotropic soil is present.

FE analyses reveal that the eccentricity factor $a = 0$ represents a best fit within the sector described by positive H and M/B values for $V/V_{max} = 1/30$, see Figure 3-6 a) and b). For a larger foundation weight, the best fit within the sector representing positive H and M/B is nevertheless achieved by applying $a = -0.15$ as presented in Figure 4-3 ($V/V_{max} = 1/6$). Experimental research and theory suggest a constant eccentricity independent of the V/V_{max} ratio, the variation in a is most likely an artifact caused by the FE code. The cross section through $V/V_{max} = 1/30$ (foundation weight (W) = 2 GN) and $V/V_{max} = 1/6$ (foundation weight (W) = 10 GN) is presented in Figure 4-3. The points illustrate FE calculation results for W = 2 GN and 10 GN respectively.

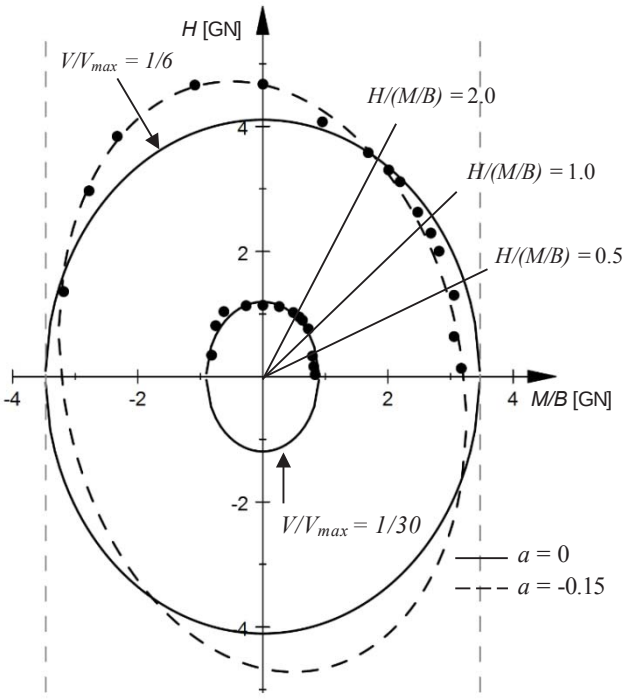

Figure 4-3. Yield surface in *H-M/B* plane. 2 GN foundation weight (constant) and 10 GN foundation weight (constant) respectively.

4.2.3 *Potential surface*

A well calibrated potential surface is generic in terms of foundation size and soil materials. The best way to verify the potential surface is to test the model towards either FE or laboratory tests. A test is therefore performed to verify the model precision. The foundation weight is kept constant = 10 GN (i.e. $V/V_{max} = 1/6$). $H / (M/B) = 2.14$ throughout the test. Other parameters are otherwise unchanged.

The result presented in Figure 4-4 shows the combined 3D (elasticity) and 2D approach adopted in this paper. The FE curve in the figure shows elastic displacements calculated by elastic stiffness parameters found from 3D FEA, whereas the plastic displacements is calculated by 2D FEA. There is a good match between the FEM

and the model results. It can be noted though that the model seems to respond somewhat stiffer compared to the results achieved at V/V_{max} = 1/30.

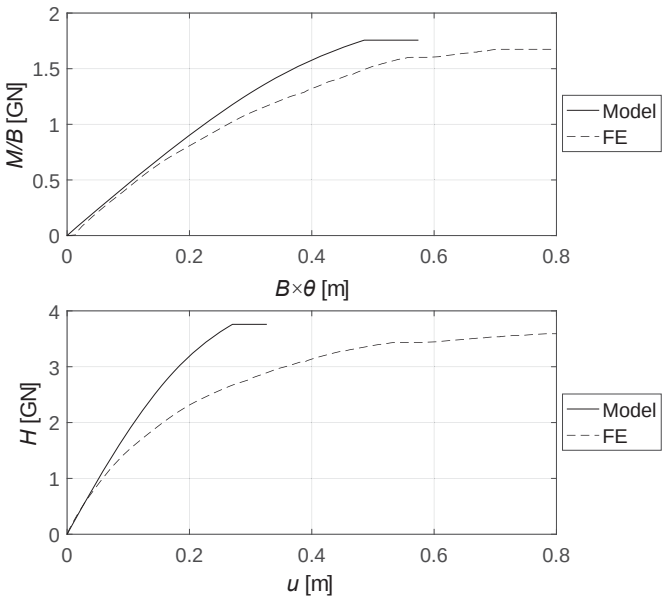

Figure 4-4. Comparison between FEM analysis and model results for Increased foundation weight, W = 10 GN. Foundation size L = 100 m, B = 50 m.

4.3 *Macro Model validation by Prototype testing*

The macro model presented herein is also validated by testing of a prototype foundation in a 4 m × 4 m × 3 m ($L \times B \times D$) sand bin. The test facilities with material properties and dimensions are documented in Tistel, et al. [46].

A 400 mm × 200 mm rectangular prototype foundation is tested for different $H/(M/B)$ ratios at V/V_{max} = 2/7.5. The model is first calibrated to FE results whereafter the macro model is used to back calculate prototype test results. The macro model results are therefore considered a "class A" prediction.

1g laboratory models of foundations on sand cannot precisely reproduce the in-situ behavior of a large foundation on sand due to size and scale effects. The laboratory testing may nevertheless reveal characteristic responses of foundations of this kind, rendering important input to accurate foundation modeling.

4.3.1 *Test rig facilities and test program*

The sand bin constitutes a 4 m × 4 m × 3 m volume of medium grained, medium dense, quartz sand from a natural glacifluvial deposit in Hokksund. The sand is air pluviated into the tank by a spreader wagon passing over the tank. The density is controlled by the size of the opening in the 462 nozzles in the spreader bottom.

The test rig is placed on top of the sand bin, and constitutes a steel frame spanning over the sand bin. The foundation arrangement is fixed to the steel frame, and can be moved along the frame allowing for several test-positions on "undisturbed" sand. This allowed for approximately 12 setup-positions on undisturbed sand before emptying and re-filling the sand-bin. Deformation is applied by ballscrews controlling the deformation in vertical and horizontal translation and in rotation. Loads response is measured by load cells. The prototype foundation and the load arrangement is shown in Figure 4-5.

Figure 4-5. Left: Picture showing the prototype foundation in the sand bin. Right: schematic overview of prototype foundation, deformation application and load measurement arrangement.

Table 7. Sand properties.

Sand property	Value
Relative density	≈73 [%]
Porosity	39.9 [%]
Variation in porosity, Δn	±0.7 [%]
Friction angle	38 [°]
Mean grain size (d_{50})	0.38 [mm]
Non-uniformity coefficient Cu = d60/d10	2.04 [-]
Density of solid particles ρ_s	2.71 [g/cm^3]
Sand density (dry sand) γ	16.0 [kN/m^3]

Testing is performed in the *H – M/B* load plane at constant *V* = 2000 N. A total of 10 Swipe tests with different *H/(M/B)* ratios are performed. The tests are deformation controlled, and the exact *H/(M/B)* ratio is therefore a result of the applied deformation.

4.3.2 *Model calibration and back calculation*

The calibration is performed in a similar manner as described within chapter 3 in this paper. Elastic parameters are calibrated to a 3D linear elastic model, and yield surface, potential surface and hardening parameters are calibrated to a 2D FE model. A hardening soil (HS) model, Schanz and Vermeer [41], is used within the FE code Plaxis. The HS parameters used in the FE code and calibrated macro model parameters are presented in Table 8 and Table 9 respectively. Further details of model calibration is provided in Tistel, et al. [46]. Best fit to a yield surface described by the FE results is found when an eccentricity factor *a* = -0.2 is applied. It is otherwise remarked that h_0 and m_0 found by swipe tests in FE are somewhat large compared to values found in literature, this is further commented in the conclusions section.

Table 8. Hardening soil parameters.

Parameter	Value
Density (dry sand) γ	16.0 [kN/m^3]
E_{50}^{ref}	15.0 [MPa]
E_{oed}^{ref}	16.7 [MPa]
E_{ur}^{ref}	30.0 [MPa]
c'_{ref}	1.2 [kPa]
φ (friction angle)	38 [°]
ψ (dilatancy angle)	8 [°]
Poisson's ratio ν	0.2 [-]
P_{ref}	100 [kPa]
K_0^{NC}	0.4 [-]
OCR	1.0 [-]

Table 9. Calibrated macro model parameters.

Yield Surface		Potential surface		Elastic Stiffness		Hardening	
h_0	0.141	h_{0p}	0.35	G	2.0 MPa	κ_0	0.28
m_0	0.11	m_{0p}	0.18	k_1	2.0	a_h	35
a	-0.2	a_p	0.0	k_2	0.4	C_1	0.5
β_{1h}	0.80	β_{1hp}	0.01	k_3	1.4	C_2	0.5
β_{2h}	0.95	β_{2hp}	0.5	k_4	-		
β_{1m}	0.95	β_{1mp}	0.95				
β_{2m}	0.99	β_{2mp}	0.8				
V_{max}	7.5 kN						

The macro model is calibrated to Eq. (37) to accommodate uplift of the foundation center at large moments. Uplift is controlled by the potential surface, thus potential surface parameters are adjusted accordingly. Back calculation of laboratory tests is performed by applying the exact same deformation path as used in the laboratory test. The FE result and calibrated macro model result is compared in Figure 4-6 a), the back-calculated macro model result and laboratory result is compared in Figure 4-6 b) and Figure 4-7.

The conclusion of the laboratory work and accompanied back calculation is that a well calibrated macro model provides a representative foundation response for a foundation loaded in the $V - M/B - H$ space as described within this paper. By inspection of Figure 4-6 it is observed that the FE model deviates somewhat (in terms of plastic stiffness) from the laboratory prototype foundation behavior, and that the macro model, which is calibrated to the FE result deviates accordingly. The FE code did not show uplift behavior, the macro model is nevertheless calibrated to accommodate uplift according to Eq. (37) and demonstrates good agreement with the observed response of the prototype foundation. It can further be concluded that the calibration by use of 3D FE for elastic behavior, and 2D FE for determination of yield surface, potential surface and hardening parameters works well. It is however remarked that there is a challenge related to definition of ultimate bearing capacity for pure vertical loading, V_{max}. The load application is limited in the test-rig, V_{max} is accordingly not found by experimental testing. A similar challenge was also met by Byrne and Houlsby [25]. Ultimate bearing capacity, V_{max}, is therefore addressed by use of 2D FE analysis. Bearing capacity of the prototype foundation is nevertheless a 3D problem as commented in section 3.2. One approach may be to use a plane strain friction angle in the 2D analysis. The plane strain friction angle might be up to 10% larger than the triaxial friction angle when the latter is in the range of 30 degrees, Meyerhof [47]. The plane strain friction angle will thereby compensate for the 3D effect (shape effect) of the prototype foundation.

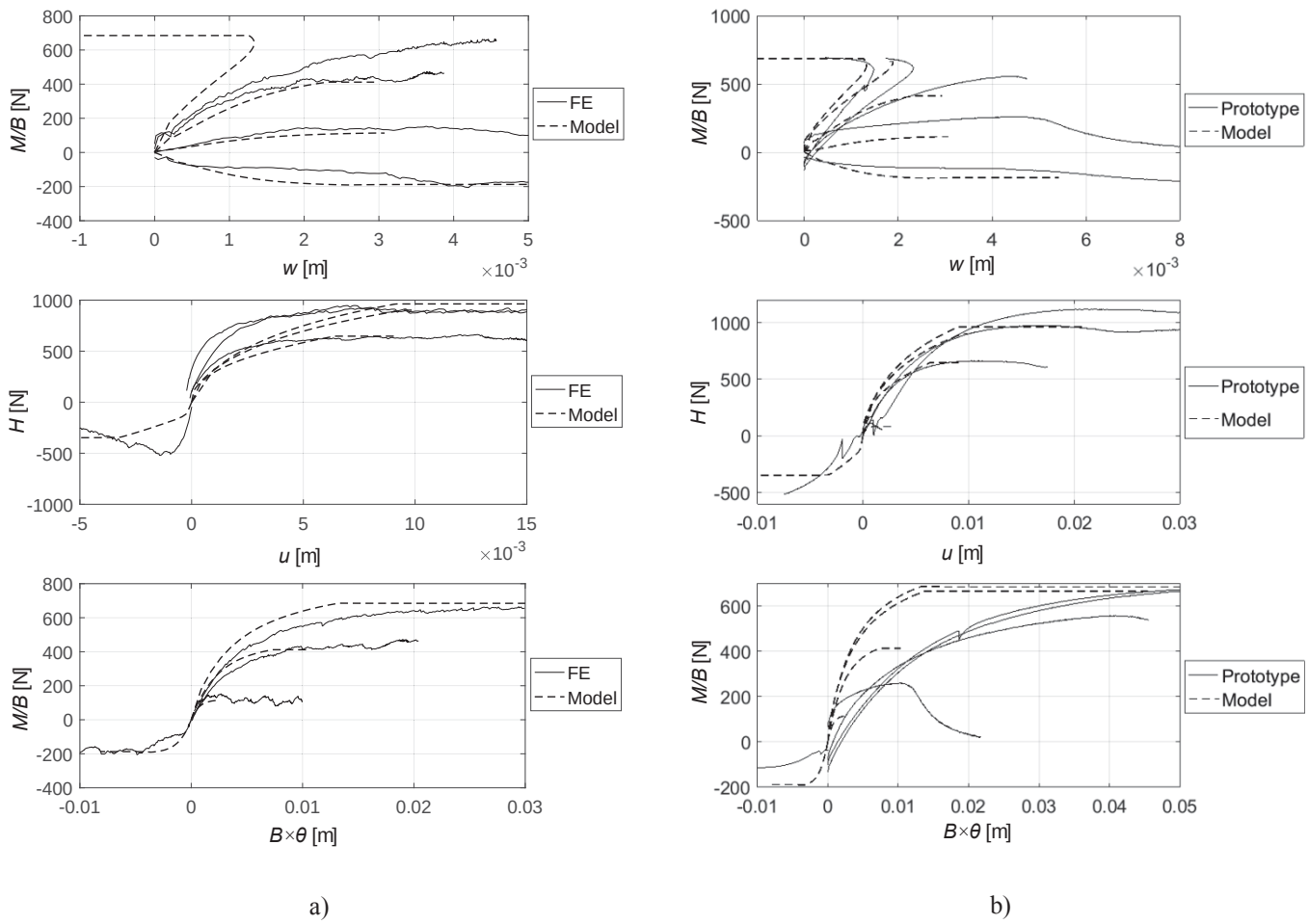

a) b)

Figure 4-6. a) FE result compared with calibrated macro model. b) macro model compared with laboratory (prototype) result.

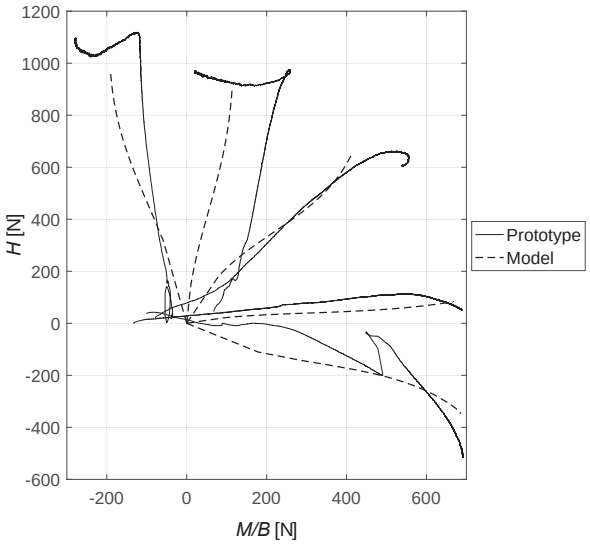

Figure 4-7. Comparison between macro model result and laboratory (prototype) result in *H – M/B* load plane.

5 Conclusion and further work

The paper outlines a macro model describing the non-linear behavior for a shallow foundation on granular material. The model is prepared for loading in one direction i.e. loads in a 2D plane. This is a reasonable approximation for structures with large load components in one direction, exemplified by a main cable anchor-block. The purpose of this paper is to present the macro model, the calibration process, and the model precision when comparing to FE results. The macro model is also validated through laboratory testing performed at the Norwegian University of Science and Technology (NTNU).

The model formulation is based on methodologies published in literature. The yield and potential surface are modified to better address the physical problems encountered for a surface foundation on granular materials. The modifications are beneficial for a case where foundation uplift due to moment occurs. The model is tested and validated for load sizes within the lower segment of V within $V < V_{max}/2$. Other models prepared for structures in sand mainly operate within the range $V/2 < V < V_{max}$ e.g. Houlsby and Cassidy [6], describing a macro model for a spud can foundation (jack-up). Within this range of V, the models can be associated (in terms of plastic flow in the V direction). The model presented within this paper is non-associated

The model demonstrates good agreement with FEA results for a broad range of load combinations. The model will show an even better match with FEA if the base case weight is larger than 2 GN as used in the calibration of the model. The example using 10 GN self weight proved a better match between the yield surface and the FE results using an eccentricity factor, a = -0.15 (Figure 4-3).

Load variations in the *H-M* plane, V and foundation size are tested. Considering the anchor block example, loading directions and actual load cases for a suspension bridge anchor block is limited bearing in mind the low variation in cable-pull throughout the lifetime. Fitting the model parameters could therefore have been performed based on a more narrow load spectra and thereby provide even more accurate results for an anchor-block assessment. Nevertheless, looking at published data, the shape parameters (h_0, m_0 and β) for the yield surface fits reasonably well with laboratory tests performed on surface foundations on sand reported by Gottardi and Butterfield [4], Martin [5] Cassidy, et al. [20] and others.

The model can be applied for a variety of surface foundations on granular materials; Gravity anchors on sand materials applied for floating structures (floating bridges, buoys etc.), subsea foundation mats on granular materials, Gravity Base Structures (GBS) and more. The model demonstrates a new application of the methodology previously developed and used within the offshore industry e.g. modeling of jack-up spudcans (Houlsby and Cassidy [6]), pipelines (Tian and Cassidy [18]), and SEPLA anchors (Cassidy [19]) to mention some of the applications.

The model is validated through 1 g prototype testing in a 4 m × 4 m × 3 m ($L \times B \times D$) sand bin. The 400 mm × 200 mm rectangular prototype foundation is tested for different *H/(M/B)* ratios at V/V_{max} = 2/7.5. The model is first calibrated to FE results whereafter the macro model is used to back calculate prototype test results. The macro model results are therefore considered a "class A" prediction. The model results demonstrate a good match with the observed prototype response, Tistel, et al. [46].

Further development to the model will consider laboratory test results for a foundation loaded at a broader range of V/V_{max}. The testing will be executed in the test-rig described in section 4.3. The test program will consider ultimate bearing capacity under pure vertical loading, swipe tests in the *H-V* plane and load paths with constant V in the *H/(M/B)* plane. The laboratory testing will address model parameters for a shallow foundation on sand.

References

[1] K. Terzaghi, *Theoretical soil mechanics*. John Wiley & Sons, New York, NY., 1943.

[2] J. Brinch-Hansen, "A Revised and Extended Formula for Bearing Capacity," Danish Geotechnical Institute, Copenhagen1970, vol. Bulletin No.98.

[3] G. G. Meyerhof, "The bearing capacity of foundations under eccentric and inclined loads," in *ICSMFE*, Zürich, 1953, vol. 1, pp. 440-445.

[4] G. Gottardi and R. Butterfield, "On the bearing capacity of surface footings on sand under general planar loads," *Soils and foundations,* vol. 33, no. 3, pp. 68-79, 1993.

[5] C. M. Martin, "Physical and numerical modelling of offshore foundations under combined loads," Doctor of Philosophy, University of Oxford, 1994.

[6] G. T. Houlsby and M. J. Cassidy, "A plasticity model for the behaviour of footings on sand under combined loading," *Géotechnique,* Research article vol. 52, no. 2, pp. 117-129, 01 March 2002 2002.

[7] C. Cremer, A. Pecker, and L. Davenne, "Modelling of Nonlinear Dynamic Behaviour of a Shallow Strip Foundation With Macro-Element," *Journal of Earthquake Engineering,* vol. 06, no. 02, pp. 175-211, 2002.

[8] K. K. Dunham, "Coastal Highway Route E39 – Extreme Crossings," *Transportation Research Procedia,* vol. 14, pp. 494-498, // 2016.

[9] O. J. Støve, Bysveen, S., Christophersen, H.P., "OTC 6882 New Foundation Systems for the Snorre Development," presented at the Offshore Technology Conference, Houston, 1992.

[10] H. K. Andersen, Dyvik, R., Schrøder, K., "Pull-Out Capacity Analyses of Suction Anchors for Tension Leg Platforms," *NGI Publication no.189,* 1993.

[11] T. Howard, B. Riley, B. Upsall, and G. Horvitz, "Structural Design of Deep Water Pontoon Mooring Anchors," in *Ports 2013*, 2013, pp. 1087-1096.

[12] G. Solland, S. Haugland, and J. Gustavsen, "The Bergsøysund Floating Bridge, Norway," presented at the Structural Engineering International, 1993.

[13] P. Meaas, E. Jordet, J. H. Gustavsen, and E. Landet, "The Salhus Floating Bridge," presented at the Fédération internationale du béton FIB Symposium-93, Kyoto, Japan, Oct.17-20, 1993, 1993.

[14] M. Yasuda, N. Furuya, and K. Hata, "Anchorages and Towers of the Akashi-Kaikyo Bridge, Japan," *Structural Engineering International,* vol. 3, no. 4, pp. 220-222, // 1993.

[15] O. Hededal and C. S. Sørensen, "Geotechnical Design Considerations for Storebælt East Bridge and Øresund High Bridge," in "AAU Geotechnical Engineering Papers: Foundation Engineering," Aalborg University, New Dehli1999.

[16] J. Tistel and G. Grimstad, "A macromodel description of the non-linear anchor block foundation behavior," in *Insights and Innovations in Structural Engineering, Mechanics and Computation Conference*, Cape Town, South Africa, 2016: Taylor & Francis group, London, 2016.

[17] B. Bienen and M. J. Cassidy, "Three-dimensional numerical analysis of centrifuge experiments on a model jack-up drilling rig on sand," *Canadian Geotechnical Journal,* vol. 46, no. 2, pp. 208-224, 2009/02/01 2009.

[18] Y. Tian and M. J. Cassidy, "Modeling of Pipe-Soil Interaction and Its Application in Numerical Simulation," *International Journal of Geomechanics,* vol. 8, no. 4, pp. 213-229, 2008.

[19] M. J. Cassidy, Gaudin, C., Randolph, M. F., Wong, P. C., Wang, D., & Tian, Y. , "A plasticity model to assess the keying of plate anchors," *Geotechnique,* vol. 62, no. 9, pp. 825-836, 2012.

[20] M. J. Cassidy, C. M. Martin, and G. T. Houlsby, "Development and application of force resultant models describing jack-up foundation behaviour," *Marine Structures,* vol. 17, no. 3–4, pp. 165-193, 5// 2004.

[21] R. Butterfield, G. T. Houlsby, and G. Gottardi, "Standardized sign conventions and notation for generally loaded foundations," *Géotechnique,* vol. 47, no. 5, pp. 1051-1054, 1997.

[22] M. Georgakis and R. Butterfield, "Displacements of footings on sand under eccentric and inclined loads," *Canadian Geotechnical Journal,* vol. 25, no. 2, pp. 199-212, 1988/05/01 1988.

[23] G. Gottardi, G. T. Houlsby, and R. Butterfield, "Plastic response of circular footings on sand under general planar loading," (in En), *Géotechnique,* vol. 49, no. 4, pp. 453-469, 1999.

[24] R. Nova and L. Montrasio, "Settlements of shallow foundations on sand," *Géotechnique,* vol. 41, no. 2, pp. 243-256, 1991.

[25] B. W. Byrne and G. T. Houlsby, "Observations of footing behaviour on loose carbonate sands," *Géotechnique,* vol. 51, no. 5, pp. 463-466, 2001.

[26] B. W. Byrne and G. T. Houlsby, "Experimental Investigations of the Response of Suction Caissons to Transient Combined Loading," *Journal of Geotechnical and Geoenvironmental Engineering,* vol. 130, no. 3, pp. 240-253, 2004.

[27] C. M. Martin and G. T. Houlsby, "Combined loading of spudcan foundations on clay: numerical modelling," *Géotechnique*, vol. 51, pp. 687-699Available: http://www.icevirtuallibrary.com/content/article/10.1680/geot.2001.51.8.687

[28] M. J. Cassidy, B. W. Byrne, and G. T. Houlsby, "Modelling the behaviour of circular footings under combined loading on loose carbonate sand," *Géotechnique*, vol. 52, pp. 705-712Available: http://www.icevirtuallibrary.com/content/article/10.1680/geot.2002.52.10.705

[29] N. Cheng and M. J. Cassidy, "Combined loading capacity of spudcan footings on loose sand," *International Journal of Physical Modelling in Geotechnics,* vol. 16, no. 1, pp. 31-44, 2016.
[30] G. T. Houlsby, "Interactions in offshore foundation design," *Géotechnique,* vol. 66, no. 10, pp. 791-825, 2016.
[31] R. Butterfield and J. Ticof, "The use of physical models in design. Discussion," *Proceedings 7th ECSMFE, Brighton,* vol. 4, pp. 259-261, 1979.
[32] R. Butterfield and G. Gottardi, "A complete three-dimensional failure envelope for shallow footings on sand," *Géotechnique,* Technical Note vol. 44, no. No.1, pp. 181-184, 1994.
[33] G. Gottardi, L. Govoni, and R. Butterfield, "Yield loci for shallow foundations by 'swipe'testing," in *Proc. Int. Symp. Frontiers in Offshore Geotech.(ISFOG), Perth*, 2005, pp. 469-475.
[34] C. L. Ngo-Tran, "The analysis of offshore foundations subjected to combined loading," University of Oxford, 1996.
[35] A. S. Veletsos and A. M. Wei, "Lateral and rocking vibration of footings," *Journal of the Soil Mechanics and Foundations Division ASCE,* vol. 97, no. 9, pp. 1227-1248, 1971.
[36] S. Bu and C. H. Lin, "Coupled horizontal-rocking impedance functions for embedded square foundations at high frequency factors," *Journal of Earthquake Engineering,* vol. 03, no. 04, pp. 561-587, 1999.
[37] M. Liingaard, L. Andersen, and L. B. Ibsen, "Impedance of flexible suction caissons," *Earthquake Engineering & Structural Dynamics,* vol. 36, no. 14, pp. 2249-2271, 2007.
[38] L. Andersen and J. Clausen, "Impedance of surface footings on layered ground," *Computers & Structures,* vol. 86, no. 1, pp. 72-87, 2008/01/01/ 2008.
[39] M. J. Cassidy, B. W. Byrne, and G. T. Houlsby, "Modelling the behaviour of circular footings under combined loading on loose carbonate sand," *Géotechnique,* vol. 52, no. 10, pp. 705-712, 2002.
[40] M. J. Cassidy, "Experimental observations of the combined loading behaviour of circular footings on loose silica sand," *Géotechnique,* vol. 57, no. 4, pp. 397-401, 2007.
[41] T. Schanz and P. A. Vermeer, "Special issue on pre-failure deformation behaviour of geomaterials," *Geotechnique,* vol. 48, pp. 383-387, 1998.
[42] A. Pais and E. Kausel, "Approximate formulas for dynamic stiffnesses of rigid foundations," *Soil Dynamics and Earthquake Engineering,* vol. 7, no. 4, pp. 213-227, 1988/10/01/ 1988.
[43] G. Gazetas, "Foundation Vibrations," in *Foundation Engineering Handbook*, H.-Y. Fang, Ed. Boston, MA: Springer US, 1991, pp. 553-593.
[44] G. Gazetas, "Analysis of machine foundation vibrations: State of the art," *International Journal of Soil Dynamics and Earthquake Engineering,* vol. 2, no. 1, pp. 2-42, 1983/01/01/ 1983.
[45] P. Wolf, *Foundation vibration analysis using simple physical models*. Swiss Federal Institute of Technology: PTR Prentice Hall, 1994.
[46] J. Tistel, G. R. Eiksund, and G. Grimstad, "Validation of a surface foundation macro model by laboratory testing (in press)," in *Offshore Site Investigation and Geotechnics Conference (OSIG)*, London, 2017.
[47] G. G. Meyerhof, "Some Recent Research on the Bearing Capacity of Foundations," *Canadian Geotechnical Journal,* vol. 1, no. 1, pp. 16-26, 1963/09/01 1963.